Available online at www.sciencedirect.com
ScienceDirect
Journal of Computational Physics 227 (2008) 7889–7916
JOURNAL OF COMPUTATIONAL PHYSICS
www.elsevier.com/locate/jcp

A wavelet-MRA-based adaptive semi-Lagrangian method for the relativistic Vlasov–Maxwell system

Nicolas Besse [a,*], Guillaume Latu [b], Alain Ghizzo [a], Eric Sonnendrücker [c], Pierre Bertrand [a]

[a] *Laboratoire de Physique des Milieux Ionisés et Applications, UMR CNRS 7040, Faculté de Sciences et Techniques, Université Henri Poincaré, Bd des Aiguillettes, B.P. 239, 54506 Vandoeuvre-lès-Nancy Cedex, France*
[b] *Laboratoire des Sciences de l'Image, de l'Informatique et de la télédétection, UMR CNRS 7005, Université Louis Pasteur, Bd Sébastien Brant, 67400 Illkirch, France*
[c] *Institut de Recherche Mathématiques Avancées, UMR CNRS 7501, Université Louis Pasteur, 7 rue René Descartes, 67084 Strasbourg, France*

Received 29 November 2006; received in revised form 28 April 2008; accepted 29 April 2008
Available online 10 May 2008

Abstract

In this paper we present a new method for the numerical solution of the relativistic Vlasov–Maxwell system on a phase-space grid using an adaptive semi-Lagrangian method. The adaptivity is performed through a wavelet multiresolution analysis, which gives a powerful and natural refinement criterion based on the local measurement of the approximation error and regularity of the distribution function. Therefore, the multiscale expansion of the distribution function allows to get a sparse representation of the data and thus save memory space and CPU time. We apply this numerical scheme to reduced Vlasov–Maxwell systems arising in laser–plasma physics. Interaction of relativistically strong laser pulses with overdense plasma slabs is investigated. These Vlasov simulations revealed a rich variety of phenomena associated with the fast particle dynamics induced by electromagnetic waves as electron trapping, particle acceleration, and electron plasma wavebreaking. However, the wavelet based adaptive method that we developed here, does not yield significant improvements compared to Vlasov solvers on a uniform mesh due to the substantial overhead that the method introduces. Nonetheless they might be a first step towards more efficient adaptive solvers based on different ideas for the grid refinement or on a more efficient implementation. Here the Vlasov simulations are performed in a two-dimensional phase-space where the development of thin filaments, strongly amplified by relativistic effects requires an important increase of the total number of points of the phase-space grid as they get finer as time goes on. The adaptive method could be more useful in cases where these thin filaments that need to be resolved are a very small fraction of the hyper-volume, which arises in higher dimensions because of the surface-to-volume scaling and the essentially one-dimensional structure of the filaments. Moreover, the main way to improve the efficiency of the adaptive method is to increase the local character in phase-space of the numerical scheme, by considering multiscale reconstruction with more compact support and by replacing the semi-Lagrangian method with more local – in space – numerical scheme as compact finite

* Corresponding author. Tel.: +33 3 836 84902; fax: +33 3 836 84933.
E-mail addresses: besse@iecn.u-nancy.fr, Nicolas.Besse@lpmi.uhp-nancy.fr (N. Besse), latu@lsiit.u-strasbg.fr (G. Latu), Alain.Ghizzo@lpmi.uhp-nancy.fr (A. Ghizzo), sonnen@math.u-strasbg.fr (E. Sonnendrücker), Pierre.Bertrand@lpmi.uhp-nancy.fr (P. Bertrand).

0021-9991/$ - see front matter
doi:10.1016/j.jcp.2008.04.031

difference schemes, discontinuous-Galerkin method or finite element residual schemes which are well suited for parallel domain decomposition techniques.

MSC: 65M15; 65P40; 83C05

Keywords: Relativistic Vlasov–Maxwell system; Multiresolution analysis; Wavelets; Laser–plasma interaction

1. Introduction

Vlasov models have long been used to study short pulse high intensity laser–plasma interaction where collisions can be ignored. This is the case for parametric instabilities, beat wave, Raman, Brillouin scattering or particle acceleration mechanisms. Since the suggestion by Tajima and Dawson [45] of particle acceleration by means of plasma waves in 1979, various schemes have been proposed to excite large amplitude electron plasma waves (EPW) (theoretically capable of reaching an electric field of the order of GV/m). Such a wave is of interest as a particle accelerator concept since electron plasma wave amplitude can largely exceed the breaking limit of the standard metallic cavity based accelerators, which is of the order of 30 MV/m.

One effective way to produce such a wave uses the forward stimulated Raman scattering (SRS) which is a stimulated decay of incident light wave (pump wave) into a scattered wave and a forward-going plasma wave [24]. The driven version of this process, the plasma beatwave accelerator (PBWA), relies upon the non-linear resonant interaction of two parallel intense laser beams [45] with a frequency difference close to the plasma frequency. In these conditions, the beat of theses two waves resonantly induces a high-phase velocity longitudinal plasma wave which traps and accelerates electrons to relativistic energies. More information can be found for instance in [23].

Intensities above $10^{19}\,\mathrm{W\,cm^{-2}}$ are reached with recently developed pulsed lasers and relativistic plasma wavebreaking can now be experimentally investigated. Particularly, one of the most interesting problems in this domain is the laser propagation through overdense plasma, in which the propagation is classically forbidden (i.e. plasmas having densities above $n_c = 1.1 \times 10^{21}\lambda_0^2\,\mathrm{cm^{-3}}$, where λ_0 is the laser wavelength in microns). However, at very high intensities, two penetration mechanisms have been considered: relativistic self-induced transparency, and conventional hole boring or forward motion of the critical surface caused by the ponderomotive pressure. Furthermore large amplitude waves can be unstable being subject to parametric instabilities. We will come back to this effect in Sections 6.1 and 6.2.

Since collisions can be ignored, the Vlasov–Maxwell system has to be used. Although very interesting analytical results are obtained from more simple fluid models such as non-linear dispersion relations, growth rates, envelope models, Manley–Rowe partition between photons, plasmons or phonons, etc., the importance of resonant wave–particle interaction leads to the use of the full kinetic relativistic Vlasov equation and furthermore to the use of numerical simulation.

However, the simulations based on the well-known Particle-In-Cell (PIC) method, have difficulty in supplying a usefully precise description of the electron acceleration process. This is because the PIC codes lack enough particles to display the detailed phase-space structure of the distribution function which is often obtained in those regions of phase-space where particle and phase velocities are comparable and where trapping occurs. For some work related to laser–plasma interaction and other tasks, using PIC code, we refer to [30,46,10].

On the other hand, direct solution of the Vlasov partial differential equation itself on a phase-space grid (the so called Vlasov codes) have been found to be a powerful tool for studying in details the particle dynamics due to the very fine resolution in phase-space [11,43,41,8,9]. For previous work concerning laser–plasma interaction using Vlasov codes we refer to [37,38,4]. Vlasov simulations are slowly introduced in place of Lagrangian PIC models for two main reasons: the lack of numerical noise and the fine resolution in velocity space, provided that the dimension of velocity space is as low as possible. This efficiency (in terms of accuracy and computational time) is however lost when filamentation takes place in phase-space which then requires an important increase of the total number of points of the phase-space grid to follow this filamentation. Usual

semi-Lagrangian Vlasov models are not well adapted to describe the Dirac-like distribution functions or fine phase-space filaments which characterize, for instance, the particle acceleration in laser–plasma interaction or the well-known phase-space filamentation in velocity of the Vlasov equation. Much progress is then expected from new adaptive time dependent grids with small mesh size in the non-zero regions and large mesh size for the sparse regions. This approach bears the promise to improve Vlasov solvers in terms of performance and accuracy. In the present work we introduce a two-dimensional phase-space mesh which can be refined or derefined adaptively in time. For this purpose we use a technique based on multiresolution analysis which is in the same spirit as the methods developed in [5,13,34]. The method was first conceived in [6] for the Vlasov–Poisson system, then used in the context of beam physics in [31,7], and parallelized with optimized data structure in [35]. In [32] the same method allows to conserve moments up to any order by using the lifting method introduced in [44].

Let us make clear however, that the wavelet based adaptive method that we developed here, does not yield significant improvements compared to Vlasov solvers on a uniform mesh due to the substantial overhead that the method introduces. Nonetheless they might be a first step towards more efficient adaptive solvers based on different ideas for the grid refinement or on a more efficient implementation.

2. PIC versus Vlasov codes

The question arises of the choice between PIC and Vlasov codes, even though PIC simulations (like any Monte Carlo method) become numerically more interesting as the dimension increases.

Before deciding which code should be the best for a given problem it must be pointed out that solving Poisson equation (or Maxwell equations) is the same task for both PIC and Vlasov codes and needs the same spatial grid, with a mesh size Δx of the order of the Debye length λ_{D}. Let N_x the number of mesh points for each spatial direction; the total number of mesh points of the spatial grid for both codes can be estimated as $(N_x)^{d_x} = (L/\Delta x)^{d_x}$ for a plasma with a typical length L, d_x being the spatial dimension of the problem ($d_x = 1$, 2 or 3).

On the other hand solving the Vlasov equation with a semi-Lagrangian method consists in a numerical computation of the characteristics ending at each mesh point (which is the equation of motion for the particles) followed by an interpolation procedure. This can be compared with a PIC solve which consists in the computation of the particle motion for each particle followed by a charge and current deposition procedure. Therefore, it is clear that pushing one particle in a PIC code needs roughly the same numerical effort as reconstructing a phase-space mesh point in an Eulerian Vlasov code.

Consequently the ratio between the numerical effort for a PIC code and a Vlasov code (CPU time as well as memory requirement) will scale as the ratio

$$\frac{N_{\mathrm{vlas}}}{N_{\mathrm{part}}},$$

where N_{vlas} is the total number of mesh points in phase-space for the Vlasov equation and N_{part} is the total number of macro-particles in the corresponding PIC code.

For a Vlasov code N_{vlas} can be written simply as the product of the spatial grid by the velocity grid

$$N_{\mathrm{vlas}} = \left(\frac{L}{\Delta x}\right)^{d_x} (N_v)^{d_v}, \tag{1}$$

where d_v is the dimension of the velocity space ($d_v = 1$, 2 or 3). Usually $d_x = d_v$ but in some cases especially when the characteristics of the Vlasov equation possess an exact invariant the two numbers may be different.

For a PIC code with a density of macro-particles n_0, N_{part} can be written

$$N_{\mathrm{part}} = n_0 L^{d_x} = n_0 (\Delta x)^{d_x} \left(\frac{L}{\Delta x}\right)^{d_x}. \tag{2}$$

In (2) $N_x^{d_x}$ can be easily recognised and we see also the appearance of $n_0 \Delta x^{d_x}$ which is nothing else but the inverse of the graininess parameter due to particle discreteness of the PIC code

$$g_{\mathrm{pic}} = \frac{1}{n_0(\lambda_{\mathrm{D}})^{d_x}}. \tag{3}$$

This relation deserves a few comments. A PIC code exhibits a paradoxical situation where the introduction of a spatial grid $\Delta x \sim \lambda_{\mathrm{D}}$ allows one to describe the collective effects through the mean field approximation but at the price of the reintroduction of individual effects due to the finite number of macro-particles. These individual effects are often considered as a numerical noise whose measure is clearly g_{pic} as given by (3). Thus keeping the coherence of the macro-particle model needs g_{pic} to be as small as possible. N_{part} can be now written

$$N_{\mathrm{part}} = g_{\mathrm{pic}}^{-1}\left(\frac{L}{\Delta x}\right)^{d_x}. \tag{4}$$

Finally from (1) and (4) we get the ratio

$$\frac{N_{\mathrm{vlas}}}{N_{\mathrm{part}}} = g_{\mathrm{pic}}(N_v)^{d_v}. \tag{5}$$

To illustrate this relation consider a typical value $N_v = 100$ which is quite reasonable to have a fine sampling of the velocity space. From (5) we can draw Table 1.

Although these numbers must be considered with caution they give the general ideas for deciding the use of PIC or Vlasov Eulerian code. Below the principal diagonal, Vlasov codes offers a better resolution at a smaller cost, while, above the diagonal, PIC codes must be preferred. To be more precise

- The use of a low g_{pic} value is needed when kinetic effects are dominant (e.g. resonant wave–particle interaction as considered). This points to the use of Vlasov codes. Moreover, in the PIC model, particles are usually loaded so as to reproduce the velocity distribution function f. It means that the velocity space resolution on a tail region of f, where resonant wave–particle interaction occurs, would be coarser than in other regions where f peaks. On the contrary, in a Vlasov code, phase-space resolution is always guaranteed, whatever the velocity profile of f.
- Finally the crucial point is the dimension of velocity space. As already demonstrated in [40] when the characteristics of the Vlasov equation possess an exact invariant a drastic reduction in velocity space can be done. This will be the case in Section 3 below. To sum up:
  - *For 1D velocity space* Vlasov codes must be preferred.
  - *For 2D velocity space* the question is open and depends on the level of noise which is bearable in the PIC code; if a small level is needed to study the onset of instabilities in laser–plasma interaction with g_{pic} smaller than 10^{-4} for instance a Vlasov code has to be used. On the contrary, for gross phenomena (where a small g_{pic} is not needed) a PIC code will do the job at a lower price.
  - *For 3D velocity space* unless the need of ultra low noise with very small g_{pic} PIC codes remain the only choice.

Actually, a 1D velocity space is relevant for some important applications to fusion plasmas. This is the case, for instance, in gyrokinetic modelling of magnetized plasmas: the recently developed gyrokinetic Vlasov code GYSELA [33] offers powerful capacities to study ion temperature gradient driven turbulence in a tokamak plasma. This is also the case (see Eq. (15)) for laser plasma interaction and obviously Vlasov codes are powerful tools to study wave–particle interaction with interesting results for trapping and action transfer from particles and waves.

Table 1
PIC code versus Vlasov code: ratio $N_{\mathrm{vlas}}/N_{\mathrm{part}}$ for $N_{\mathrm{v}} = 100$

	$d_{\mathrm{v}} = 1$	$d_{\mathrm{v}} = 2$	$d_{\mathrm{v}} = 3$
$g_{\mathrm{pic}} = 10^{-2}$	**1**	10^{2}	10^{4}
$g_{\mathrm{pic}} = 10^{-4}$	10^{-2}	**1**	10^{2}
$g_{\mathrm{pic}} = 10^{-6}$	10^{-4}	10^{-2}	**1**

Table 2
PIC code versus Vlasov code: ratio $N_{\text{vlas}}/N_{\text{part}}$ for $N_{\text{v}} = 1000$

	$d_{\text{v}} = 1$	$d_{\text{v}} = 2$	$d_{\text{v}} = 3$
$g_{\text{pic}} = 10^{-2}$	*10*	10^4	10^7
$g_{\text{pic}} = 10^{-4}$	10^{-1}	10^2	10^5
$g_{\text{pic}} = 10^{-6}$	10^{-3}	*1*	10^3

Nevertheless we would point out the problem of simulating ultra high intensity lasers. Due to strong acceleration, it may happen that most of the particles are localized in tiny regions of phase-space while large regions are empty of particles. Very fine grids are needed and the number of mesh points in velocity space must be greater than the value considered in Table 1.

Clearly for those mesh points where f is close to zero, the computer is spending a lot of CPU time in computing only zeros. For instance if filamentation is thin enough to require a finer velocity resolution with $N_v = 1000$ instead of $N_v = 100$, results are less in favor of Vlasov codes as seen in Table 2.

This is a major drawback of Vlasov methods using a uniform and fixed mesh.

Since the non-zero regions evolve continuously with time, there is the need to have adaptive time dependent grids with small mesh size in the non-zero regions and large mesh size for the sparse regions. This would decrease N_v to more interesting values for Vlasov simulation purpose.

This paper might be considered as a first attempt to investigate the possible use of adaptive techniques especially when the interesting physical phenomena occur in a localized phase-space region and do not require a fine mesh everywhere. The adaptive method can be overlaid to the classical semi-Lagrangian method which is based on the conservation of the distribution function along particle trajectories. The phase-space mesh can be updated using a multiresolution technique as wavelet expansion, which gives a sparse representation and a natural criterion to perform local grid refinements.

Our last remark, before we concentrate on the adaptive mesh Vlasov code, is that this general approach is also valid for non-neutral plasmas. Non-neutral plasmas, like electrically neutral plasma, exhibit a broad range of collective properties as equivalent Debye shielding, the fundamental role being played by the confinement (electric or magnetic) fields. An appropriate thermal Debye length may be introduced for the equilibrium constructed in the presence of the confinement fields. Basic theoretical studies of one component pure electron plasmas showed that collective oscillation properties of non-neutral plasma [17–19] are directly analogous to the collective properties of neutral plasma, as long as the equilibrium self-field effects due to the space charge are appropriately modified.

3. The relativistic Vlasov–Maxwell model

In this section we present the reduced relativistic Vlasov–Maxwell model that we want to solve numerically. We aim at describing the behavior of an electromagnetic wave propagating in a relativistic electron gas in a fixed neutralizing ion background. Here we consider a one-dimensional plasma in space along the x-direction. Since non-linear kinetic effects are important in laser–plasma interaction, we choose a kinetic description for the plasma, which implies to solve a Vlasov equation for a four-dimensional distribution function $\mathcal{F} = \mathcal{F}(t, x, p_x, p_y, p_z)$

$$\frac{\partial \mathcal{F}}{\partial t} + \frac{p_x}{m\gamma}\frac{\partial \mathcal{F}}{\partial x} + e\left(\mathbf{E} + \frac{\mathbf{p}\times\mathbf{B}}{m\gamma}\right)\cdot\frac{\partial \mathcal{F}}{\partial \mathbf{p}} = 0, \tag{6}$$

where $\mathbf{p} = (p_x, p_y, p_z)$ is the momentum variable, $(\mathbf{E}, \mathbf{B})$ the electromagnetic field and γ the Lorentz factor

$$\gamma^2 = 1 + \frac{p_x^2 + p_y^2 + p_z^2}{m^2c^2}. \tag{7}$$

We now reduce the four-dimensional Vlasov equation to a two-dimensional Vlasov equation by using the invariants of the system. The Hamiltonian of a relativistic particle in the electromagnetic field $(\mathbf{E}, \mathbf{B})$ for a one-dimensional spatial system reads

$$\mathcal{H} = mc^2\left(1 + \frac{(\mathbf{P}_c - e\mathbf{A})^2}{m^2c^2}\right)^{1/2} + e\phi(t,x), \tag{8}$$

where ϕ is the electrostatic potential, $\mathbf{A}$ the vector potential, and $\mathbf{P}_c$ the canonical momentum related to the particle momentum $\mathbf{p}$ by $\mathbf{P}_c = \mathbf{p} + e\mathbf{A}$. In order that the field is well determined by the potentials we have to add a gauge. We choose the Coulomb gauge ($\operatorname{div}\mathbf{A} = 0$), which implies that $\mathbf{A} = \mathbf{A}_\perp(t,x)$. If we write the Hamilton equation

$$\frac{\mathrm{d}\mathbf{P}_c}{\mathrm{d}t} = -\frac{\partial\mathcal{H}}{\partial\mathbf{q}},$$

with $\mathbf{q} = (x,y,z)$, then along the longitudinal x-direction of propagation of the electromagnetic wave we have

$$\frac{\mathrm{d}\mathbf{P}_{cx}}{\mathrm{d}t} = -\frac{\partial\mathcal{H}}{\partial x}, \tag{9}$$

and for the transverse (y,z)-direction

$$\frac{\mathrm{d}\mathbf{P}_{c\perp}}{\mathrm{d}t} = -\partial_\perp\mathcal{H} = 0. \tag{10}$$

The Eq. (10) means $\mathbf{P}_{c\perp} = \text{constant} = \mathcal{P}_{c\perp}$ and $\mathbf{P}_{c\perp}$ is no more an independent or free variable but a parameter. Therefore the structure of the solution is of the form

$$\mathcal{F}(t,x,p_x,\mathbf{p}_\perp) = \int_{\mathcal{P}_{c\perp}} f(t,x,p_x,\mathcal{P}_{c\perp})\delta(\mathbf{p}_\perp - (\mathcal{P}_{c\perp} - e\mathbf{A}_\perp))\,\mathrm{d}\mathcal{P}_{c\perp},$$

where $\mathcal{P}_{c\perp}$ has to be understood as a parameter or a label in f. Since the parameter $\mathcal{P}_{c\perp}$ is associated to an invariant of the system we can consider a coarse sampling of it, which implies a substantial reduction of the numerical effort. Therefore we can mimic a perpendicular temperature profile (recovering of transverse kinetic effects) or study various beam interaction systems. On the contrary, the independent variables (x,p_x) are associated to local partial differential operators, thus we need sufficiently dense sampling of them. Therefore, without loss of generality, we now consider a plasma initially prepared so that particles are divided into $\mathcal{N}$ bunches of particles, each bunch i, $1 \leqslant i \leqslant \mathcal{N}$ having the same initial perpendicular canonical momentum $\mathbf{P}_{c\perp} = \mathcal{P}_{c\perp,i}$. From (9) the i-particles have any longitudinal p_x with a distribution $f_i(t,x,p_x)$. The Hamiltonian of one particle of bunch i is given by

$$\mathcal{H}_i(t,x,p_x) = mc^2(\gamma_i(t,x,p_x) - 1) + e\phi(t,x) \tag{11}$$

with the corresponding γ_i Lorentz factor

$$\gamma_i^2 = 1 + \frac{p_x^2}{m^2c^2} + \frac{(\mathcal{P}_{c\perp,i} - e\mathbf{A}_\perp(t,x))^2}{m^2c^2}. \tag{12}$$

Each group i is described by a distribution function $f_i(t,x,p_x)$ which must obey the Vlasov equation

$$\frac{\mathrm{d}f_i}{\mathrm{d}t} = \frac{\partial f_i}{\partial t} + [\mathcal{H}_i, f_i] = 0, \quad i = 1\ldots\mathcal{N}, \tag{13}$$

where $[\cdot,\cdot]$ is the Poisson bracket in (x,p_x) variables, namely $[\varphi,\psi] = \partial_{p_x}\varphi\partial_x\psi - \partial_x\varphi\partial_{p_x}\psi$. Eqs. (11)–(13) lead to

$$\frac{\partial f_i}{\partial t} + \frac{p_x}{m\gamma_i}\frac{\partial f_i}{\partial x} + \left(eE_x + \frac{1}{2m\gamma_i}\frac{\partial}{\partial x}(\mathcal{P}_{c\perp,i} - e\mathbf{A}_\perp(t,x))^2\right)\frac{\partial f_i}{\partial p_x} = 0, \quad i = 1\ldots\mathcal{N} \tag{14}$$

and the structure of the solution is now

$$\mathcal{F}(t,x,p_x,\mathbf{p}_\perp) = \sum_{i=1}^{\mathcal{N}} f_i(t,x,p_x)\delta(\mathbf{p}_\perp - (\mathcal{P}_{c\perp,i} - e\mathbf{A}_\perp)), \tag{15}$$

thus reducing a four-dimensional phase-space to a two-dimensional one (plus $\mathcal{N}$ values $\mathcal{P}_{c\perp,i}$ for the invariant $\mathbf{P}_{c\perp}$). We now add the Maxwell equations which couple the different f_i through the scalar potential ϕ and the

potential vector $\mathbf{A}_\perp$. The one-dimensional wave-propagation model allows to separate the electric field into two parts, namely $\mathbf{E} = E_x\mathbf{e}_x + \mathbf{E}_\perp$, where $E_x = -\partial_x\phi$ is a pure electrostatic field, which obeys Poisson's equation, and $\mathbf{E}_\perp = -\partial_t\mathbf{A}_\perp$ is a pure electromagnetic field. In absence of any external magnetic field, $\mathbf{B}$ is purely perpendicular and is given by $\mathbf{B}_\perp = \nabla \times \mathbf{A}_\perp$. The two Maxwell equations $\nabla \times \mathbf{E} + \partial_t\mathbf{B} = 0$ and $\nabla \cdot \mathbf{B} = 0$ are automatically satisfied. The two others couple the f_i. The Maxwell–Gauss equation $\partial_x E_x = \rho/\varepsilon_0$ becomes

$$\frac{\partial E_x}{\partial x} = \frac{e}{\varepsilon_0}\left(\sum_{i=1}^{\mathcal{N}} n_i(t,x) - n_0\right), \tag{16}$$

where the charge density n_i of the bunch i is defined by

$$n_i(t,x) = \int_{-\infty}^{\infty} f_i(t,x,p_x)\,\mathrm{d}p_x. \tag{17}$$

Let us notice that we can equivalently replace the Poisson's equation by the longitudinal x-component of the Ampère equation to compute E_x,

$$\frac{\partial E_x}{\partial t} = -\frac{1}{\varepsilon_0}\sum_{i=1}^{\mathcal{N}} J_{x,i}(t,x), \tag{18}$$

where the current density $J_{x,i}$ of the bunch i is defined by

$$J_{x,i}(t,x) = \frac{e}{m}\int_{-\infty}^{\infty} p_x f_i(t,x,p_x)\frac{\mathrm{d}p_x}{\gamma_i}. \tag{19}$$

Introducing the propagator fields $E^\pm = E_y \pm cB_z$ and $F^\pm = E_z \pm c\ B_y$, the Maxwell–Ampère equations $\nabla \times \mathbf{B}_\perp = \mu_0(\mathbf{J}_\perp + \varepsilon_0\partial_t\mathbf{E}_\perp)$ give the transport equations

$$\frac{\partial E^\pm}{\partial t} \pm c\frac{\partial E^\pm}{\partial x} = -\frac{1}{\varepsilon_0}\sum_{i=1}^{\mathcal{N}} J_{y,i}, \tag{20}$$

$$\frac{\partial F^\pm}{\partial t} \mp c\frac{\partial F^\pm}{\partial x} = -\frac{1}{\varepsilon_0}\sum_{i=1}^{\mathcal{N}} J_{z,i}, \tag{21}$$

where the current density $\mathbf{J}_{\perp,i} = (J_{y,i}, J_{z,i})$ is defined by

$$\mathbf{J}_{\perp,i}(t,x) = \frac{e}{m}(\mathcal{P}_{c\perp,i} - e\mathbf{A}_\perp))\int_{-\infty}^{\infty} f_i(t,x,p_x)\frac{\mathrm{d}p_x}{\gamma_i}. \tag{22}$$

Let us notice that the Eqs. (20) and (21) can be integrated exactly along their vacuum characteristics $x \pm ct =$ constant if we can integrate exactly the source term $\mathbf{J}_\perp$. In the sequel we will consider the particular case $\mathcal{N} = 1$, thus from (15) it corresponds to a cold plasma distribution in the perpendicular direction. Since usually no streaming effects are considered we take $\mathcal{P}_{c\perp,1} = 0$. In the context of laser–plasma interaction, this is consistent with the fact that particle acceleration and heating is very strong in the longitudinal laser direction with temperature $T_\parallel \gg T_\perp$, provided that the transverse Weibel instability may be neglected.

4. The wavelet multiresolution analysis

This section introduces the ideas and the main tool, the wavelet multiresolution analysis (MRA), we use to construct our adaptive numerical scheme. We first present the framework of bi-orthogonal wavelets introduced in [14], because it shows how our scheme can be extended to any wavelet which enters within this framework, and it gives also a better theoretical understanding of the way to construct our adaptive method. Afterwards, we describe the special bi-orthogonal wavelet we have used for our simulation: the interpolet. Then we can reinterpret the method as a prediction–projection process. Finally, in order to take benefit of adaptivity, we have to compute in an adaptive fashion the fluid moments of the distribution function (charge and current densities). This task should be cautiously looked into.

4.1. The bi-orthogonal wavelet framework

Bi-orthogonal wavelets such as interpolating and orthonormal wavelets, can be obtained in a systematic way, once we are given a pair of dual scaling function. Thus the main theoretical difficulties in the construction of wavelet bases mostly reside in the selection of an appropriate pair of dual scaling functions which possess the desired properties for the analysis (oscillations, vanishing moments, singularities localization, compact support, refinability), and for the reconstruction (smoothness, high-order accuracy approximation, stability, compact support). The scaling function φ and its dual counterpart $\tilde{\varphi}$ are refinable functions which satisfy the following refinement equations

$$\varphi(x) = \sqrt{2}\sum_{n\in\mathbb{Z}} h_n \varphi(2x-n), \quad \text{and} \quad \tilde{\varphi}(x) = \sqrt{2}\sum_{n\in\mathbb{Z}} \tilde{h}_n \tilde{\varphi}(2x-n), \tag{23}$$

where the coefficient sequences $\{h_n\}_{n\in\mathbb{Z}}$ and $\{\tilde{h}_n\}_{n\in\mathbb{Z}}$, called filters, are given (or have to be constructed such that the refinement equations (23) are satisfied). We define new coefficients

$$g_n = (-1)^{n+1}\tilde{h}_{1-n} \quad \text{and} \quad \tilde{g}_n = (-1)^{n+1} h_{1-n}, \tag{24}$$

and a pair of dual wavelets by

$$\psi(x) = \sqrt{2}\sum_{n\in\mathbb{Z}} g_n \varphi(2x-n), \quad \text{and} \quad \tilde{\psi}(x) = \sqrt{2}\sum_{n\in\mathbb{Z}} \tilde{g}_n \tilde{\varphi}(2x-n). \tag{25}$$

Moreover the pair of dual scaling functions $(\varphi, \tilde{\varphi})$ and wavelet functions $(\psi, \tilde{\psi})$ satisfy orthogonal relations (stability properties), more precisely

$$\begin{aligned} &\langle \psi(\cdot), \tilde{\psi}(\cdot - k)\rangle = \delta_{0,k}, \quad \langle \psi(\cdot), \tilde{\varphi}(\cdot - k)\rangle = 0, \\ &\langle \varphi(\cdot), \tilde{\varphi}(\cdot - k)\rangle = \delta_{0,k}, \quad \langle \tilde{\psi}(\cdot), \varphi(\cdot - k)\rangle = 0, \end{aligned} \tag{26}$$

where $\langle \cdot, \cdot \rangle$ denotes the duality bracket between two functions, one belonging to a functional space $\mathcal{S}$ and the other in the dual space $\mathcal{S}'$, i.e.

$$\langle \varphi, \psi \rangle = \int_{\mathbb{R}} \varphi(x)\psi(x)\,\mathrm{d}x.$$

The orthogonality equations (26) imply some "orthogonality" relations that the filters must also satisfy, namely

$$\begin{aligned} &\sum_{n\in\mathbb{Z}} h_n \tilde{h}_{n+2k} = \sum_{n\in\mathbb{Z}} g_n \tilde{g}_{n+2k} = \delta_{0,k}, \\ &\sum_{n\in\mathbb{Z}} h_n \tilde{g}_{n+2k} = \sum_{n\in\mathbb{Z}} g_n \tilde{h}_{n+2k} = 0. \end{aligned} \tag{27}$$

If we use the notations $\varphi_k^j(\cdot) = 2^{j/2}\varphi(2^j\cdot - k), \tilde{\varphi}_k^j(\cdot) = 2^{j/2}\tilde{\varphi}(2^j\cdot - k), \psi_k^j(\cdot) = 2^{j/2}\psi(2^j\cdot - k), \tilde{\psi}_k^j(\cdot) = 2^{j/2}\tilde{\psi}(2^j\cdot - k)$ and if we define $V_j = \mathrm{Span}\{\varphi_k^j\}_{k\in\mathbb{Z}}$, $\widetilde{V}_j = \mathrm{Span}\{\tilde{\varphi}_k^j\}_{k\in\mathbb{Z}}$, $W_j = \mathrm{Span}\{\psi_k^j\}_{k\in\mathbb{Z}}$, $\widetilde{W}_j = \mathrm{Span}\{\tilde{\psi}_k^j\}_{k\in\mathbb{Z}}$, then from orthogonality relations (26) we have the following spaces decompositions

$$\begin{aligned} &V_{j+1} = V_j \oplus W_j, \qquad V_{j+1} = V_{\mathring{j}} \oplus W_{\mathring{j}} \oplus \cdots \oplus W_j, \\ &\widetilde{V}_{j+1} = \widetilde{V}_j \oplus \widetilde{W}_j, \qquad \widetilde{V}_{j+1} = \widetilde{V}_{\mathring{j}} \oplus \widetilde{W}_{\mathring{j}} \oplus \cdots \oplus \widetilde{W}_j, \end{aligned}$$

with $\mathring{j} \in \mathbb{Z}$ and where $W_j \perp W_i$ if $i \neq j$ and $\tilde{W}_j \perp \tilde{W}_i$ if $i \neq j$. The spaces V_j are defined on the dyadic grids $G_j = \{x_k^j = k2^{-j}, k \in \mathbb{Z}\}$ and satisfy the inclusions $\{0\} \subset \cdots \subset V_j \subset V_{j+1} \subset \cdots \subset L^2$. From the previous spaces decompositions a function $f_{j+1} = P_{j+1}f \in V_{j+1}$ can be expressed on either basis

$$\begin{aligned} f_{j+1} = P_{j+1}f &= \sum_{k\in\mathbb{Z}} c_k^{j+1}\varphi_k^{j+1} = \sum_{k\in\mathbb{Z}} c_k^j \varphi_k^j + \sum_{k\in\mathbb{Z}} d_k^j \psi_k^j = P_j f + \sum_{k\in\mathbb{Z}} d_k^j \psi_k^j = \sum_{k\in\mathbb{Z}} c_k^{\mathring{j}}\varphi_k^{\mathring{j}} + \sum_{l=\mathring{j}}^{j}\sum_{k\in\mathbb{Z}} d_k^l \psi_k^l \\ &= \sum_{l\leqslant j}\sum_{k\in\mathbb{Z}} d_k^l \psi_k^l \end{aligned}$$

with $c_k^j = \langle f, \tilde{\varphi}_k^j \rangle, d_k^j = \langle f, \tilde{\psi}_k^j \rangle$, and where P_j denotes the projection operator onto V_j. As we work at least on a two-dimensional phase-space we have to generalize univariate wavelets to multivariate wavelets, which can be done by tensor product construction. A d-dimensional multiresolution analysis can be constructed from a 1-dimensional multiresolution analysis by tensor products as follows

$$\mathcal{V}_j = (\otimes)^n V_j.$$

If we define $\Sigma = \{\varepsilon = (\varepsilon_1, \ldots, \varepsilon_d) \in \mathbb{Z}^d, \varepsilon \neq 0, \varepsilon_i \in \{0,1\}, i = 1 \ldots d\}$, then we get the space decomposition

$$\mathcal{V}_j = \mathcal{V}_{j-1} \bigoplus_{\varepsilon \in \Sigma} \mathcal{W}_{j-1}^{\varepsilon},$$

where $\mathcal{W}_{j-1}^{\varepsilon} = U_{j-1}^{\varepsilon_1} \otimes \cdots \otimes U_{j-1}^{\varepsilon_d}$ with $U_{j-1}^{i} = \begin{cases} V_{j-1} & \text{if } i = 0, \\ W_{j-1} & \text{if } i = 1. \end{cases}$

Using the notations $x = (x_1, \ldots, x_d)$ and $k = (k_1, \ldots, k_d)$ the projection of a function f onto $\mathcal{V}_J$ can be decomposed as

$$f_J(x) = \sum_{k \in \mathbb{Z}^d} c_k^{\mathring{j}} \psi_k^{0,\mathring{j}}(x) + \sum_{j=\mathring{j}}^{J-1} \sum_{\varepsilon \in \Sigma} \sum_{k \in \mathbb{Z}^d} d_k^{\varepsilon,j} \psi_k^{\varepsilon,j}(x),$$

where $\psi_k^{\varepsilon,j}(x) = \psi_{k_1}^{i_1,j}(x_1) \cdots \psi_{k_d}^{i_d,j}(x_d)$ with $\psi_k^{i,j} = \begin{cases} \varphi_k^j & \text{if } i = 0, \\ \psi_k^j & \text{if } i = 1. \end{cases}$

For an exhaustive overview on wavelets and its applications in numerical analysis we refer to [15,12] and references therein.

4.2. Interpolating wavelets: interpolets

In this section we describe the bi-orthogonal wavelet that we choose to build our scheme, namely an interpolating wavelet based on Lagrange interpolating polynomials. In fact this interpolating wavelets (interpolets) are based on an interpolating subdivision scheme whose task is to build an interpolant for a given data sequence. For example we are given a sequence of samples of some unknown function at regular intervals and the task is to fill intermediate values in a smooth way. The iterative Lagrangian interpolation scheme, first introduced in the works of Deslauriers and Dubuc [20,21], solves this problem by defining a recursive procedure for finding the values of an interpolating function at all dyadic points. This algorithm proceeds by inserting a predicted coefficient between each pair of existing coefficients. Since none of the already existing coefficients are changed, interpolation of the original function is preserved. This recursive subdivision process is extensively used in CAGD to generate curves and surfaces, see for example the 4-points scheme [22]. In fact some interpolating subdivision schemes as the 4-points scheme or the Deslauriers–Dubuc method fall into the framework of bi-orthogonal wavelets. Let us see how. For this purpose the filter sequences defining our pair of dual scaling and wavelet functions are chosen such that

$$h_{2n} = \delta_{0,n}, \quad \tilde{h}_n = \delta_{0,n}, \quad \tilde{g}_{2n+1} = \delta_{0,n}, \quad \tilde{g}_{2n} = -a_n, \tag{28}$$

where the coefficients a_n have to be prescribed. In Table 3, we give some examples of values of a_n for interpolating polynomials P_{2N-1} of degree $2N-1$ for $N = 1, 2, 3$, and the pictures of the pairs of dual scaling and wavelet functions represented by Figs. 1–3.

Using the bi-orthogonality relations (26), the refinement equations (23) and (25) and the filter sequences (28) we get

Table 3
Coefficients of interpolating polynomial for different values of N

$N = 1$	$a_0 = a_1 = \frac{1}{2}, a_n = 0$ else
$N = 2$	$a_{-1} = a_2 = -\frac{1}{16}, a_0 = a_1 = \frac{9}{16}, a_n = 0$ else
$N = 3$	$a_{-2} = a_3 = \frac{3}{256}, a_{-1} = a_2 = -\frac{25}{256}, a_0 = a_1 = \frac{75}{128}, a_n = 0$ else

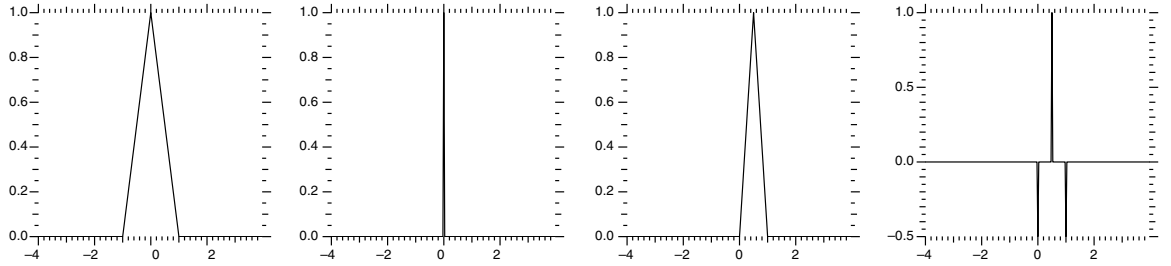

Fig. 1. Pairs of dual scaling and wavelets functions for $N = 1$.

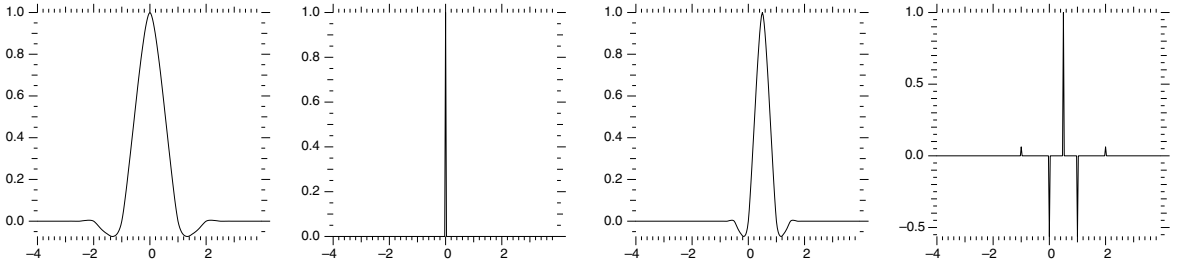

Fig. 2. Pairs of dual scaling and wavelets functions for $N = 2$.

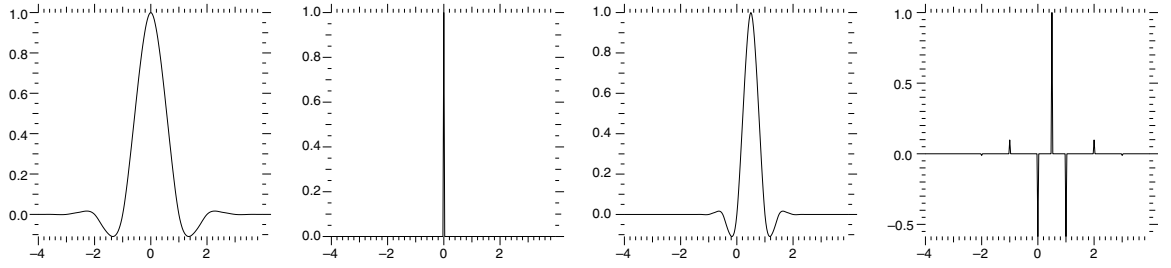

Fig. 3. Pairs of dual scaling and wavelets functions for $N = 3$.

$$
\begin{aligned}
c_k^j &= \langle f_{j+1}, \tilde{\varphi}_k^j \rangle = \sum_{n,l\in\mathbb{Z}} c_n^{j+1} \tilde{h}_{l-2k} \langle \varphi_n^{j+1}, \tilde{\varphi}_l^{j+1} \rangle = \sum_{n\in\mathbb{Z}} c_n^{j+1} \tilde{h}_{n-2k} = c_{2k}^{j+1}, \\
d_k^j &= \langle f_{j+1}, \tilde{\psi}_k^j \rangle = \sum_{n,l\in\mathbb{Z}} c_n^{j+1} \tilde{g}_{l-2k} \langle \varphi_n^{j+1}, \tilde{\varphi}_l^{j+1} \rangle = \sum_{n\in\mathbb{Z}} c_{2n+2k}^{j+1} \tilde{g}_{2n} + c_{2n+2k+1}^{j+1} \tilde{g}_{2n+1} \\
&= c_{2k+1}^{j+1} - \sum_{n=1-N}^{N} a_n c_{2n+2k}^{j+1} = c_{2k+1}^{j+1} - \sum_{n=1-N}^{N} a_n c_{n+k}^{j} = c_{2k+1}^{j+1} - P_{2N-1}(x_{2k+1}^{j+1}),
\end{aligned}
$$

where P_{2N-1} stands for the Lagrange interpolation polynomial of odd degree $2N-1$ centered at the point (x_{2k+1}^{j+1}). Therefore d_k^j represents exactly the difference between the value of the function in the space V_{j+1} and the value predicted from V_j. This strategy for constructing W_j is particularly interesting for adaptive refinement as d_k^j will be small where the prediction from V_j is good and large elsewhere, thus it gives a natural refinement criterion.

Furthermore we can map a function defined on a dyadic grid from one level to the next by a prediction operator $\mathcal{P}_j^{j+1}$ or map a function defined on a dyadic grid from one level to the previous by projection (or restriction) operator $\mathcal{P}_{j+1}^j$. If we consider two dyadic grids G_j and G_{j+1} then, the prediction and projection operators which allow to go from the sequence $\{c_k^j\}_{k\in\mathbb{Z}}$ to the sequence $\{c_k^{j+1}\}_{k\in\mathbb{Z}}$ and vice versa are defined as

$$\begin{aligned}
\mathcal{P}_{j+1}^{j}: \quad & G_{j+1} && \to && G_j \\
& \{c_k^{j+1}\}_{\{k\in\mathbb{Z}\}} && \mapsto && \{c_k^j | c_k^j = c_{2k}^{j+1}\}_{\{k\in\mathbb{Z}\}}
\end{aligned}$$

$$\mathcal{P}_{j}^{j+1}: \quad G_j \to G_{j+1}$$

$$\{c_k^j\}_{\{k\in\mathbb{Z}\}} \mapsto \left\{ \left. \begin{array}{l|lll} c_k^{j+1} & c_{2k}^{j+1} & = & c_k^j \\ & c_{2k+1}^{j+1} & = & P_{2N-1}(x_{2k+1}^{j+1}) \\ & & = & \sum_n a_n c_{n+k}^j \end{array} \right. \right\}_{\{k\in\mathbb{Z}\}}$$

Let us note that $\tilde{\varphi}(x) = \delta(x)$ is not in L^2 but in the set of Radon measures. The wavelet function ψ can be easily deduced from φ. Indeed, as $g_n = (-1)^{n+1}\tilde{h}_{1-n}$, we have $g_n = \delta_{1,n}$ and thus using the refinement equation (25) we have $\psi_k^j(x) = \varphi_{2k+1}^{j+1}(x)$. The scaling function φ shares the following properties:

(i) *Compact support*: φ is exactly zero outside the interval $[-2N+1, 2N-1]$.
(ii) *Interpolation*: φ is interpolating by construction in the sense that $\varphi(k) = \delta_{0,k}$.
(ii) *Polynomial reconstruction and high-order accuracy*: polynomials up to degree $2N-1$ can be expressed as a linear combination of scaling functions, more precisely
$$\sum_{k\in\mathbb{Z}} (k2^{-j})^q \varphi_k^j(x) = x^q, \quad \text{for } 0 \leqslant q < 2N.$$
(iii) *Smoothness*: We have typically $\varphi \in \mathcal{C}^\alpha$, where $\alpha = \alpha(N)$. We know that $\alpha(2) < 2$ and that $\alpha(N)$ increases linearly with N. For more details on smoothness analysis of wavelets we refer to [12,15].

4.3. Thresholding, adaptivity and optimality

The multiresolution analysis allows to decompose a function $f_{j+1} = P_{j+1}f \in \mathcal{V}_{j+1}$ into its low-frequency part on the coarser dyadic grid $\mathcal{V}_j$ and its high-frequency part on the supplementary spaces $\{\mathcal{W}_j^\varepsilon\}_{\varepsilon\in\Sigma}$ of $\mathcal{V}_j$ in $\mathcal{V}_{j+1}$. Therefore the spaces $\{\mathcal{W}_j^\varepsilon\}_{\varepsilon\in\Sigma}$ contain the details $d_k^{\varepsilon,j}$ needed to improve the approximation given in the space $\mathcal{V}_j$ and obtain a finer approximation in the space $\mathcal{V}_{j+1}$. If the detail $d_k^{\varepsilon,j}$ is large, then the improvement is locally important around the point $2^{-(j+1)}(2k+1)$ and conversely if it is small, then the local improvement is also small and thus it can be neglected without losing too much approximation quality. Therefore the multiscale representation of a function of $\mathcal{V}_{j+1}$ can be compressed with a controlled approximation loss by setting to zero the details with an absolute value less than some given threshold ϵ_j depending on the level j. As we have seen in the previous section, the size of the detail coefficients $d_k^{\varepsilon,j}$ is also associated to the local approximation error of the prediction operator (equivalent to an interpolation scheme) and consequently it is related to the local regularity of the function which is approximated. Hence large detail $d_k^{\varepsilon,j}$ means that the prediction operator gives a bad approximation of the function, locally around the point $2^{-(j+1)}(2k+1)$ because the regularity of the function is locally weak (oscillations in the case of Vlasov equation). In order to get a better approximation some supplementary points should be added around the point $2^{-(j+1)}(2k+1)$. The approximation $P_{j+1}f$ of f, on the bases of $\mathcal{V}_j$ and $\{\mathcal{W}_j^\varepsilon\}_{\varepsilon\in\Sigma}$ reads

$$f_{j+1}(x) = P_{j+1}f(x) = \sum_{k\in\mathbb{Z}^d} c_k^j \psi_k^{0,j}(x) + \sum_{\varepsilon\in\Sigma}\sum_{k\in\mathbb{Z}^d} d_k^{\varepsilon,j}\psi_k^{\varepsilon,j}(x).$$

Let ϵ_j be a given threshold. If we eliminate all the details smaller than the threshold then we get a new approximation

$$\hat{f}_{j+1} = \sum_{k\in\mathbb{Z}^d} c_k^j \psi_k^{0,j} + \sum_{\varepsilon\in\Sigma}\sum_{\{k|d_k^{\varepsilon,j}\geqslant\epsilon_j\}} d_k^{\varepsilon,j}\psi_k^{\varepsilon,j}.$$

Assuming that f_{j+1} has compact support, the number of removed terms is finite and thus the error induced by this thresholding process can be bounded in L^p-norm ($1 \leqslant p < \infty$)

$$\left\| \sum_{\{k|d_k^{\varepsilon,j}<\epsilon_j\}} \sum_{\varepsilon\in\Sigma} d_k^{\varepsilon,j}\psi_k^{\varepsilon,j} \right\|_{L^p} \lesssim 2^{jd(1/2-1/p)} \left\| \{d_k^{\varepsilon,j}\}_{(k,\varepsilon)\in\{(i,\eta)|d_i^{\eta,j}<\epsilon_j\}} \right\|_{\ell^p} \lesssim \epsilon_j 2^{jd(1/2-1/p)} (\#\{(k,\varepsilon)|d_k^{\varepsilon,j} < \epsilon_j\})^{1/p},$$

where $\#E$ denotes the cardinality of the finite set E.

The thresholds ϵ_j should be chosen in order to remain within the accuracy which is achieved by the non-adaptive scheme while reducing the CPU time and memory storage. To this end, we need to control the thresholding error and the prediction (or refinement) error with a prescribed precision ϵ. Therefore, we will be able to control the global error in time and space with respect to the reference scheme (its non-adaptive version) up to the prescribed accuracy ϵ. For the thresholding error, if we set $\epsilon_j = 2^{-jd(1/2-1/p)}\epsilon_0$, we obtain the bound

$$\left\| \sum_{j=\mathring{j}}^{J} \sum_{\{k|d_k^{\varepsilon,j}<\epsilon_j\}} \sum_{\varepsilon\in\Sigma} d_k^{\varepsilon,j}\psi_k^{\varepsilon,j} \right\|_{L^p} \lesssim \left\| \{2^{jd(1/2-1/p)} d_k^{\varepsilon,j}\}_{(k,\varepsilon,j)\in\{(i,\eta,l)|2^{ld(1/2-1/p)}d_i^{\eta,l}<\epsilon_0\}} \right\|_{\ell^p}. \tag{29}$$

A first crude estimate of (29) is given by $\epsilon_0 \# G_J$ which suggests the choice $\epsilon_0 = \epsilon 2^{-dJ}$. A sharper estimate is given by $\epsilon_0 \# \widehat{G}^n_{\epsilon_0}$ (see Section 5 for the definition of $\widehat{G}^n_{\epsilon_0}$) which leads to the time dependent threshold

$$\epsilon_0 = \epsilon(\#\widehat{G}^n_{\epsilon_0})^{-1}. \tag{30}$$

A better choice is to take the largest ϵ_0 such that

$$\left\| \{2^{jd(1/2-1/p)} d_k^{\varepsilon,j}\}_{(k,\varepsilon,j)\in\{(i,\eta,l)|2^{ld(1/2-1/p)}d_i^{\eta,l}<\epsilon_0\}} \right\|_{\ell^p} \leqslant \epsilon. \tag{31}$$

For the refinement error, we would like to define $\widehat{G}^n_{\epsilon_0}$ in such a way that

$$\left| d_k^{\varepsilon,j}(\mathring{f}^n_{G_J}) \right| < \epsilon_j \quad \text{if } (k,\varepsilon,j) \notin \widehat{G}^n_{\epsilon_0}, \tag{32}$$

where $\mathring{f}^n_{G_J}$ stands for the distribution function computed on the mesh G_J, by using a Δt-computation step of the non-adaptive semi-Lagrangian scheme (i.e. by dropping the Step 3, 4 and 6 in the algorithm described in Section 5) with the compressed wavelet decomposition f^n, known on the adaptive mesh $G^n_{\epsilon_0}$, as initial condition. The detail $d_k^{\varepsilon,j}(\mathring{f}^n_{G_J})$ is the wavelet coefficient of the function $\mathring{f}^n_{G_J}$ at the point (k,ε,j). For non-linear evolution operators, we need to rely on specifically adapted refinement or prediction rules. For example, in the context of the numerical approximation of hyperbolic problems by Eulerian methods (finite volume schemes), with cell average multiresolution decompositions, the following rules were proposed by Harten in [36]: (i) If $|d_k^{\varepsilon,j,n}| > \epsilon_j$, with $d_k^{\varepsilon,j,n}$ the wavelet coefficient of the unknown at time t^n and at the point (k,ε,j), then we include in new adaptive mesh the immediate neighbors of the point (k,ε,j) at the same level. (ii) If $|d_k^{\varepsilon,j,n}| > 2^{r-1}\epsilon_j$, with r the order of accuracy of the prediction operator, then we also include the children at the finer level (i.e. refine by one level the corresponding cell of the adaptive grid). These rules are derived heuristically. Although they are satisfactory in practice, these rules do not seem to be sufficient to prove estimate like the inequality (32). In [13], a more severe refinement rule is proposed: refine by q levels if $2^{q(s-1)} \leqslant |d_k^{\varepsilon,j}| < 2^{(q+1)(s-1)}$, with s the Hölder smoothness of the underlying continuous wavelet system $\{\psi_k^{\varepsilon}\}_{(k\in\mathbb{Z},\varepsilon\in\Sigma)}$ obtained as the limit of $\{\psi_k^{\varepsilon,J}\}_{(k\in\mathbb{Z},\varepsilon\in\Sigma)}$ by letting $J\to\infty$. With such a rule the authors of [13] succeed to prove estimate like the inequality (32). In practice, it is nevertheless observed that Harten's rule [36] is sufficient and that the thresholding error tend to dominate the refinement error. If we suppose that the estimates (30) or (31) and (32) hold, and provided that the discrete numerical transport operator-constructed in the non-adaptive semi-Lagrangian scheme – and the projection operator P_j have good stability properties in L^p spaces, with a stability constant bounded at worst by $1 + C\Delta t$ (C being a constant independent of the discretization parameters), then the global error estimate – in L^p-norm – between the exact solution and that given by the adaptive semi-Lagrangian numerical scheme behave like $\mathcal{O}(\Delta t^k + (h^{m+1}+\epsilon)/\Delta t)$, where $k+1$ is the order of the local trunction error in time of the non-adaptive scheme, and m is the degree of the polynomial that can be reconstructed by linear combination of wavelet functions, and with $h \sim 2^{-J}$ the minimum radius of the cells.

For our adaptive semi-Lagrangian scheme (see Section 5, Step 3) our refinement strategy, is inspired by Harten's rule. In fact we proceed as follows: (i) If $|d_k^{\varepsilon,j,n}| > \epsilon_j$, we advect the associated point $(k,\varepsilon,j) \in G^n_{\epsilon_0}$ by pushing forward the characteristics coming from this point (k,ε,j) during a time Δt. To this end we integrate the characteristic curves with a forward Euler scheme. Then we include the immediate neighbors of the ending point at the same level j. (ii) If $|d_k^{\varepsilon,j,n}| > 2^{r-1}\epsilon_j$, with $r \in \mathbb{N}$ (here $r = 2$), we also include the children of the target cell at the finer level $j+1$ (i.e. refine by one level the corresponding cell – of level j – in which the ending point of the characteristic curve falls). This rule leads to the construction of the mesh $\widetilde{G}^n_{\epsilon_0}$ (see Section 5,

Step 3). Even if this rule is heuristic, as the Harten ones, it supplies good results in practice as it can be observed on the numerical simulations of the Section 6. As a conclusion of this section, let us note that a complete analysis of the exact trade-off between accuracy and complexity (represented by the number of parameters $\#G_{\epsilon_0}^n$) and then a proof of the optimality of the adaptive strategy are still not available, even for very simple equations such as one-dimensional scalar conservation laws, for which theoretical results such as Theorem 1.1 in [16] indicate the adaptive methods should behave significantly better than non-adaptive methods.

4.4. Computation of the moments

In order to take benefit of the adaptivity, we have to compute the charge and the current density in an adaptive fashion. Thus, we intend to suppress any computation that takes place on the finest grid. For this purpose, it is natural to replace in Eqs. (17), (19) and (22) the distribution function by its multiscale decomposition. Nevertheless in the integrals (19) and (22) there are non-linear terms in p_x because of the presence of the Lorentz factor $\gamma_1(t,x,p_x)$. To overcome this problem one answer is to project the non-linear term $\gamma_1(t,x,p_x)$ onto a set of local polynomials. More precisely we suppose first that we can compute with any precision the moments of φ and ψ:

$$m_k^{\varphi} = \int \varphi(p) p^k \,\mathrm{d}p, \quad m_k^{\psi} = \int \psi(p) p^k \,\mathrm{d}p.$$

Let us consider the two-dimensional wavelet decomposition of the approximation f_{j+1} of f in the space V_{j+1}

$$f_{j+1}(x,p_x) = \sum_{(k_1,k_2)\in\mathbb{Z}^2} \left(c_{k_1,k_2}^{\hat{j}} \varphi_{k_1}^{\hat{j}}(x) \varphi_{k_2}^{\hat{j}}(p_x) + \sum_{q=\hat{j}}^{j} \left(d_{k_1,k_2}^{r,q} \psi_{k_1}^{q}(x) \varphi_{k_2}^{q}(p_x) + d_{k_1,k_2}^{c,q} \varphi_{k_1}^{q}(x) \psi_{k_2}^{q}(p_x) + d_{k_1,k_2}^{m,q} \psi_{k_1}^{q}(x) \psi_{k_2}^{q}(p_x) \right) \right). \tag{33}$$

Using the decomposition formula (33), projecting $\gamma_1^{-1}(x,p_x)$ on local polynomials in p_x of degree Q, after integration the equations (17), (19) and (22) will lead to

$$\begin{aligned}
n_{j+1}(x) &= \int f_{j+1}(x,p_x)\,\mathrm{d}p_x = F_n(x, m_0^{\varphi}, m_0^{\psi}),\\
J_{x,j+1}(x) &= \frac{e}{m} \int f_{j+1}(x,p_x) \frac{p_x \,\mathrm{d}p_x}{\gamma_1(x,p_x)} = F_{J_x}(x, m_0^{\varphi}, m_0^{\psi}, \ldots, m_{Q+1}^{\varphi}, m_{Q+1}^{\psi}),\\
\mathbf{J}_{\perp,j+1}(x) &= -\frac{e^2 \mathbf{A}_{\perp}}{m} \int f_{j+1}(x,p_x) \frac{\mathrm{d}p_x}{\gamma_1(x,p_x)} = F_{J_{\perp}}(x, m_0^{\varphi}, m_0^{\psi}, \ldots, m_Q^{\varphi}, m_Q^{\psi}).
\end{aligned}$$

Now let us explicit the functions F_n, F_{J_x} and $F_{J_{\perp}}$ in the case of Lagrange polynomials of degree two and three. In the section of the interpolet description we have seen that we can deduce the wavelet function from the scaling function by the relation $\psi_k^j(\cdot) = \varphi_{2k+1}^{j+1}(\cdot)$. Hence we only consider the case of the scaling function φ_k^j. Let us take the basis $\{p_1,p_2,p_3\}$ of one-dimension Lagrange polynomials of degree two centered at the point $2^{-j}l$ with support $[(-2N+1+l)2^{-j},(2N-1+l)2^{-j}]$. Let $\{q_1,q_2,q_3,q_4\}$ the basis of one-dimension Lagrange polynomials of degree three centered at the same point with the same support. More precisely we have

$$\begin{aligned}
p_1(\cdot) &= \frac{2^{2j-1}}{(2N-1)^2}(\cdot - 2^{-j}l)(\cdot - 2^{-j}(l+2N-1)),\\
p_2(\cdot) &= -\frac{2^{2j}}{(2N-1)^2}(\cdot - 2^{-j}(-2N+1+l))(\cdot - 2^{-j}(l+2N-1)),\\
p_3(\cdot) &= -\frac{2^{2j-1}}{(2N-1)^2}(\cdot - 2^{-j}(-2N+1+l))(\cdot - 2^{-j}l),
\end{aligned}$$

$$q_1(\cdot) = -\frac{3^2 2^{3j-4}}{(2N-1)^3}\left(\cdot - 2^{-j}\left(\frac{1-2N}{3}+l\right)\right)\left(\cdot - 2^{-j}\left(\frac{2N-1}{3}+l\right)\right)(\cdot - 2^{-j}(2N-1+l)),$$

$$q_2(\cdot) = \frac{3^3 2^{3j-4}}{(2N-1)^3}(\cdot - 2^{-j}(1-2N+l))\left(\cdot - 2^{-j}\left(\frac{1-2N}{3}+l\right)\right)(\cdot - 2^{-j}(2N-1+l)),$$

$$q_3(\cdot) = -\frac{3^3 2^{3j-4}}{(2N-1)^3}(\cdot - 2^{-j}(1-2N+l))\left(\cdot - 2^{-j}\left(\frac{1-2N}{3}+l\right)\right)(\cdot - 2^{-j}(2N-1+l)),$$

$$q_4(\cdot) = \frac{3^2 2^{3j-4}}{(2N-1)^3}(\cdot - 2^{-j}(1-2N+l))\left(\cdot - 2^{-j}\left(\frac{1-2N}{3}+l\right)\right)\left(\cdot - 2^{-j}\left(\frac{2N-1}{3}+l\right)\right).$$

If we interpolate $\gamma_1^{-1}(x,p_x)$ in the local bases $\{p_1,p_2,p_3\}$ and $\{q_1,q_2,q_3,q_4\}$, after some algebra we find

$$n_{j+1}(x) = \sum_{k_1,k_2\in\mathbb{Z}^2}\left(2^{-\mathring{j}}c^{\mathring{j}}_{k_1,k_2}\varphi^{\mathring{j}}_{k_1}(x) + \sum_{q=\mathring{j}}^{j}\left(2^{-j}d^{r,q}_{k_1,k_2}\psi^q_{k_1}(x) + 2^{-(j+1)}d^{c,q}_{k_1,k_2}\varphi^q_{k_1}(x) + 2^{-(j+1)}d^{m,q}_{k_1,k_2}\psi^q_{k_1}(x)\right)\right), \tag{34}$$

$$J_{x,j+1}(x) = \frac{e}{m}\sum_{k_1,k_2\in\mathbb{Z}^2}\left(c^{\mathring{j}}_{k_1,k_2}w^{\mathring{j}}_{1,k_2}(x)\varphi^{\mathring{j}}_{k_1}(x) + \sum_{q=\mathring{j}}^{j}\left(d^{r,q}_{k_1,k_2}w^j_{1,k_2}(x)\psi^q_{k_1}(x) + d^{c,q}_{k_1,k_2}w^{j+1}_{1,2k_2+1}(x)\varphi^q_{k_1}(x) + d^{m,q}_{k_1,k_2}w^{j+1}_{1,2k_2+1}(x)\psi^q_{k_1}(x)\right)\right), \tag{35}$$

$$\mathbf{J}_{\perp,j+1}(x) = -\frac{e^2\mathbf{A}_\perp}{m}\sum_{k_1,k_2\in\mathbb{Z}^2}\left(c^{\mathring{j}}_{k_1,k_2}w^{\mathring{j}}_{2,k_2}(x)\varphi^{\mathring{j}}_{k_1}(x) + \sum_{q=\mathring{j}}^{j}\left(d^{r,q}_{k_1,k_2}w^j_{2,k_2}(x)\psi^q_{k_1}(x) + d^{c,q}_{k_1,k_2}w^{j+1}_{2,2k_2+1}(x)\varphi^q_{k_1}(x) + d^{m,q}_{k_1,k_2}w^{j+1}_{2,2k_2+1}(x)\psi^q_{k_1}(x)\right)\right). \tag{36}$$

For the case of quadratic Lagrange polynomials we have

$$w^j_{2,l}(x) = \frac{2^{-j}}{2^3}m_2^\varphi\left(\frac{\alpha^j_{-3,l}(x)+\alpha^j_{3,l}(x)}{2}\right) + 2^{-j}\left(1-\frac{m_2^\varphi}{2^3}\right)\alpha^j_{0,l}(x),$$

$$w^j_{1,l}(x) = 2^{-j}lw^j_{2,l}(x) + \frac{2^{-2j}}{3}m_2^\varphi\left(\frac{\alpha^j_{3,l}(x)-\alpha^j_{-3,l}(x)}{2}\right)$$

and for the case of cubic Lagrange polynomials we have

$$w^j_{2,l}(x) = \frac{2^{-j}}{2^4}(m_2^\varphi-1)\left(\alpha^j_{-3,l}(x)+\alpha^j_{3,l}(x)\right) + \frac{3^2 2^{-j}}{2^4}\left(1-\frac{m_2^\varphi}{2^3}\right)\left(\alpha^j_{-1,l}(x)+\alpha^j_{1,l}(x)\right),$$

$$w^j_{1,l}(x) = 2^{-j}lw^j_{2,l}(x) + 2^{-2j}\left\{\frac{(m_4^\varphi-m_2^\varphi)}{2^4 3}\left(\alpha^j_{3,l}(x)-\alpha^j_{-3,l}(x)\right) + \frac{(m_4^\varphi-3^2m_2^\varphi)}{2^4}\left(\alpha^j_{-1,l}(x)-\alpha^j_{1,l}(x)\right)\right\},$$

where $\alpha^j_{i,l}(x) = \gamma_1^{-1}(x,2^{-j}(l+i))$. Therefore, the computation of n_{j+1}, $J_{x,j+1}$, and $\mathbf{J}_{\perp,j+1}$ require a number of operations linear in the number of non-zero details $d^j_{k_1,k_2}$ and $c^j_{k_1,k_2}$ coefficients.

5. The adaptive numerical approximation

This section is devoted to the description of the global adaptive algorithm.

Step 1. **Initialisation**. Let $\mathring{j}$ be the level of the coarsest dyadic grid and J the level of the finest one. In the initialisation phase, we first compute the wavelet decomposition of the initial condition f_0 which is known analytically. It is then compressed by eliminating the details which are smaller than the threshold ϵ_0 (in L^1-norm, i.e. $p=1$ in (29)) that we set. We then construct an adaptive mesh, named $G^0_{\epsilon_0}$.

From all the possible points at the levels between our coarsest and finest, the mesh $G^0_{\epsilon_0}$ contains only those of the coarsest and those corresponding to details which are above the given threshold ϵ_0. From the compressed wavelet decomposition of f_0 we compute all the moments ρ^0, J^0_x and $\mathbf{J}^0_\perp$ using the method depicted in Section 4.4. Solving the Poisson equation (16) we obtain a value for E^0_x. Therefore we get $E^{1/2}_x$ by solving the Ampère equation (18) following the scheme $E^{1/2}_x(x) = E^0_x(x) - \Delta t J^0_x/(2\varepsilon_0)$. Furthermore we suppose that we know analytical expressions for $E^{\pm,0}$, $F^{\pm,0}$, $E^{\pm,-1/2}$, $F^{\pm,-1/2}$ and $\mathbf{A}^0_\perp$. All these assumptions allow to start the code self-consistently. In fact the quantities E_x, $E^\pm$, $F^\pm$ are computed at time $t^{n-1/2}$ and the quantities f, $\mathbf{A}_\perp$ are computed at time t^n. We now suppose that we know the quantities $E^{n-1/2}_x, E^{\pm,n-1/2}, F^{\pm,n-1/2}, f^n, \mathbf{A}^n_\perp$, and $\widetilde{G}^n$ then the following numerical scheme allows to get the same quantities one time step further.

Step 2. **Electromagnetic field integration**. From the compressed wavelet decomposition f^n known on the adaptive mesh $G^n_{\epsilon_0}$ we compute adaptively (cf. Section 4.4) the moments ρ^n, J^n_x and $\mathbf{J}^n_\perp$. Therefore the fields $(E^{\pm,n+1/2}, F^{\pm,n+1/2})$ and $E^{n+1/2}_x$ are computed by integrating, respectively Eqs. (20) and (21) along their vacuum characteristics $x \pm ct =$ constant and the Ampère equation (18) on the time interval $[t^{n-1/2}, t^{n+1/2}]$ using a second order quadrature rule in time (middle point rule), i.e.

$$E^{n+1/2}_x(x) = E^{n-1/2}_x(x) - \Delta t J^n_x(x)/\varepsilon_0,$$
$$E^{\pm,n+1/2}(x \pm c\Delta t) = E^{\pm,n-1/2}(x) - \Delta t J^n_y(x \pm c\Delta t/2)/\varepsilon_0,$$
$$F^{\pm,n+1/2}(x \mp c\Delta t) = F^{\pm,n-1/2}(x) - \Delta t J^n_z(x \mp c\Delta t/2)/\varepsilon_0.$$

Hence we may integrate exactly along the vacuum characteristics using grid spacing $\Delta x = c\Delta t$, and consequently we have

$$J^n_y(x \pm c\Delta t/2) = \frac{1}{2}(J^n_y(x \pm \Delta x) + J^n_y(x)), \quad J^n_z(x \mp c\Delta t/2) = \frac{1}{2}(J^n_z(x \mp \Delta x) + J^n_z(x)).$$

For the prediction step we will need to know $(E^{\pm,n}, F^{\pm,n})$ and E^n_x. They are approximated by averaging, i.e.

$$E^n_x(x) = \frac{1}{2}(E^{n-1/2}_x(x) + E^{n+1/2}_x(x))$$

and

$$E^{\pm,n}(x) = \frac{1}{2}(E^{\pm,n-1/2}(x) + E^{\pm,n+1/2}(x)), \quad F^{\pm,n}(x) = \frac{1}{2}(F^{\pm,n-1/2}(x) + F^{\pm,n+1/2}(x)).$$

Step 3. **Prediction**. We predict the positions of the phase-space (x, p_x) points where the details should be important at the next time t^{n+1} by pushing forward the characteristics coming from the points of the mesh $G^n_{\epsilon_0}$. This new mesh is denoted by $\widetilde{G}^n_{\epsilon_0}$. To this purpose we use a simple Euler scheme for time integration, i.e.

$$z^{n+1} = z^n + \Delta t F(t^n, z^n),$$

where

$$z(t) = (x(t), p_x(t)), \quad F(t, z(t)) = \left(\frac{p_x(t)}{m\gamma_1(t, x(t), p_x(t))}, e\left(E_x(t, x(t)) - \frac{(\mathbf{A}_\perp \times \mathbf{B}_\perp)(t, x(t))}{\gamma_1(t, x(t), p_x(t))}\right)\right),$$

with the notation $z^n = z(t^n)$. In order to capture new fine scales and new physical phenomena, we retain the mesh points, at one level finer than the starting point, whose support contains the end characteristic point (see Section 4.3).

Step 4. **Construction of the mesh** $\widehat{G}^n_{\epsilon_0}$. From the predicted mesh $\widetilde{G}^n_{\epsilon_0}$, we construct the mesh $\widehat{G}^n_{\epsilon_0}$ where the values of the distribution function at the next time step shall be computed. Since the mesh $\widetilde{G}^n_{\epsilon_0}$ is not suitable to perform a wavelet decomposition, we construct the well formed tree $\widehat{G}^n_{\epsilon_0}$ which contains exactly the points necessary for computing the wavelet transform of f^{n+1} at the points of $\widetilde{G}^n_{\epsilon_0}$.

Step 5. **Transport-interpolation**. First we need to compute $\mathbf{A}_\perp^{n+1/2}$. To this purpose we use a time centered scheme to solve $\partial_t \mathbf{A}_\perp = -\mathbf{E}_\perp$. Hence we get

$$\mathbf{A}_\perp^{n+1}(x) = \mathbf{A}_\perp^n(x) - \Delta t \mathbf{E}_\perp^{n+1/2}(x),$$

and finally we obtain $\mathbf{A}_\perp^{n+1/2}(x)$ by the averaging

$$\mathbf{A}_\perp^{n+1/2}(x) = \frac{1}{2}(\mathbf{A}_\perp^{n+1}(x) + \mathbf{A}_\perp^n(x)).$$

Now we push backwards the characteristic curves which end at the points of $\widehat{G}_{\epsilon_0}^n$ on a time step Δt, to find the origin of these characteristic curves, namely z^n. Integrating the non-linear ODE $d_t z(t) = F(t, z(t))$ on the time interval $[t^n, t^{n+1}]$, using a middle point quadrature rule and the second order in time approximation $z^{n+1/2} = (z^{n+1} + z^n)/2$ we are leading to solve the fixed-point problem in δz

$$\delta z = \Delta t F(t^{n+1/2}, z^{n+1} - \delta z/2),$$

where we set $\delta z = z^{n+1} - z^n$. This fixed-point problem can be easily solved by a Newton algorithm. Then we interpolate the distribution function at the origin of the characteristic curves by using the wavelet decomposition f^n on the mesh $G_{\epsilon_0}^n$, to update the distribution function f^{n+1} on the mesh $\widehat{G}_{\epsilon_0}^n$.

Step 6. **Wavelet transform and compression**. We compute the new coefficient sequences $\{c_k^{j,n+1}\}_{k\in\mathbb{Z}^2}$, $\{d_k^{\ell,n+1}\}_{k\in\mathbb{Z}^2,\ell\in[j,J-1]}$ at the points of $\widetilde{G}_{\epsilon_0}^n$ from the values of f^{n+1} known at the points of $\widehat{G}_{\epsilon_0}^n$. Hence we eliminate the points of $\widetilde{G}_{\epsilon_0}^n$ where the details $d_k^{\ell,n+1}$ are lower than the level dependent threshold $\epsilon_\ell = 2^{-\ell d(1/2-1/p)}\epsilon_0$ (in L^1-norm, i.e. $p = 1$ in (29)), and thus we obtain the new adaptive mesh $G_{\epsilon_0}^{n+1}$. Finally we close the loop of a Δt-computation step by going back to step 2.

6. Simulations of laser–plasma interaction

In order to show the efficiency of our algorithm and its high accuracy some simulations have been carried out to analyse in detail the wave–particle dynamics met in the relativistic regime of the laser–plasma interaction with moderately overdense plasma. When electromagnetic waves propagate through a plasma layer, they become parametrically unstable. At low densities, they are identified as the stimulated Raman scattering (SRS). At large intensities, strong relativistic effects give rise to the longitudinal relativistic modulational instability (RMI) and the transverse relativistic filamentation instability (RFI). For such instabilities the growth rates are so high ($\gamma/\omega_p \gtrsim 0.3$) that these instabilities start from the round-off errors of the numerical scheme (when no initial perturbation is introduced).

The Vlasov equation, coupled to the Poisson or Maxwell equation, often leads to the filamentation process, which is one of the reasons why Vlasov simulations have been poorly considered, compared to PIC simulations which are not sensitive to this problem. The distribution function is constant along the characteristic curves which tend to roll up, so that the phase-space regions where the distribution function has different values, come close together and steep gradients are thus generated. Vlasov simulations provide an excellent description of the small scales of the phase-space dynamics, although the well-known filamentation mechanism and phase-space mixing are saturated by the numerical dissipation of the numerical scheme. Indeed, there exists a time when the phase-space grid becomes too coarse to follow these thin filaments which get finer as time goes on. Furthermore this mechanism is electromagnetic strongly amplified by relativistic effects since parametric instabilities (RMI, RFI) tend naturally to produce thin filaments via strong particle acceleration.

6.1. The relativistic parametric instability

In this section, we check the numerical method by computing the vortices induced by the relativistic modulational instability generated by an ultra-intense pump wave in a periodic box. In this test case, the pump electromagnetic wave is assumed to be circularly polarized with a dispersion relation given by $\omega_0^2 = \omega_p^2/\gamma_0 + k_0^2 c^2$, (ω_0, k_0) being respectively, the pump frequency and the wave number of the electromagnetic wave, and γ_0 being given by $\gamma_0^2 = 1 + p_{\text{osc}}^2/m^2c^2 = 1 + a_0^2$. Let us note that Akhiezer and Polovin [2] find a solution to this problem for

the propagation of a circularly polarized transverse electromagnetic wave in a homogeneous plasma, i.e. such that $f(t,x,p_x) = n_0 F_0(p_x)$. A large amplitude right ($v = +1$) circularly polarized electromagnetic wave is initialized in a simulation box with a quiver momentum $a_0 = p_{\rm osc}/mc = \sqrt{3}$ and we have chosen

$$E_y(t=0,x) = E_0 \cos(k_0 x), \quad E_z(t=0,x) = vE_0 \sin(k_0 x).$$

The initial condition for the magnetic components has been taken as

$$B_y(t=0,x) = -vE_0 \frac{k_0}{\omega_0} \sin(k_0 x), \quad B_z(t=0,x) = E_0 \frac{k_0}{\omega_0} \cos(k_0 x).$$

The corresponding initial condition for the transverse potential vector $\mathbf{A}_\perp$, are then given by

$$A_y(t=0,x) = \frac{E_0}{\omega_0} \sin(k_0 x), \quad A_z(t=0,x) = -v\frac{E_0}{\omega_0} \cos(k_0 x).$$

The pump wave frequency is $\omega_0 = 1\omega_p$ corresponding to a wave number $k_0 c/\omega_p = 2\Delta k/\omega_p = 1/\sqrt{2}$, $\Delta\, l = 2\pi/L_x$ being the fundamental mode of the plasma corresponding to a ratio of the plasma density to the critical density of $n_0/n_c = 1$. The numerical integration was carried out with a time step $\omega_p \Delta t = 0.017355$. The phase-space sampling is chosen as follows. We choose the coarsest level as $\mathring{\jmath}_x = 6, \mathring{\jmath}_{p_x} = 7$, and the finest level of refinement as $J_x = 9, J_{p_x} = 10$, which means that we allow three levels of adaptive refinement. In other words we choose a coarse grid $N_x N_{p_x} = 64 \times 128$ with the possibility to refine the mesh adaptively on three more levels. The threshold ϵ_0 is set to 10^{-6}.

Large amplitude plane light (ω_0, k_0) couples any existing plasma fluctuation (ω, k) to a hierarchy of electromagnetic sidebands $(\omega_0 + \ell\omega, k_0 + \ell k)$. At low intensities ($a_0 \ll 1$), Stimulated Raman Scattering, the decay into a resonant electron plasma wave and Stokes (with $\ell = -1$) and possibly anti-Stokes ($\ell = +1$) electromagnetic sidebands, is the dominant mechanism. At large intensity ($a_0 \gtrsim 1$), the different ℓ becomes strongly coupled with the growth of several plasma modes (ω, k), known as relativistic parametric instabilities [29]. In the cold plasma case we have $F_0(p_x) = \delta(p_x)$ and the Vlasov equation reduces to fluid equations. Assuming (ω_0, k_0) is the dominant mode and (ω, k) a small perturbation, a little algebra yields the dispersion relation (see [29]):

$$D_+ D_- = \frac{\omega_p^2 a_0^2}{\gamma_0^3} \left(\frac{k^2 c^2}{D_p} - 1 \right) (D_+ + D_-), \tag{37}$$

where D_p, $D_\pm$ correspond respectively to the dispersion relation of the electron plasma wave and of the electromagnetic waves in the presence of the large amplitude electromagnetic wave. We have

$$D_p = \omega^2 - \frac{\omega_p^2}{\gamma_0} \tag{38}$$

with $\gamma_0 = (1 + a_0^2)^{\frac{1}{2}}$ and

$$D_\pm = (\omega \pm \omega_0)^2 - (k \pm k_0)^2 c^2 - \frac{\omega_p^2}{\gamma_0}. \tag{39}$$

The temperature of initial distribution function of the plasma is chosen such that the cold plasma approximation is still valid. In fact this approximation consists in neglecting the longitudinal thermal velocity compared to the quiver velocity of the electron, being close to light speed, i.e. $v_{\rm th}/c = \sqrt{(k_{\rm B} T_\parallel / m_e)}/c = 0.044\sqrt{T_\parallel\ [\rm keV]} \ll 1$. In this numerical example we take a Maxwellian equilibrium with $T_\parallel = 3$ keV, i.e, $v_{\rm th} = \sqrt{3/511}$. The numerical resolution of the dispersion equation (37)–(39), gives a maximum growth rate $\gamma/\omega_p = 0.409$ at $k_{\max} c/\omega_p = 1.469$. The numerical growth rate is *0.403*, thus less than 1.5% of error. In Fig. 4 we can see the time evolution of the electric energy. As no initial perturbation has been introduced in the distribution function, the method being noiseless, the longitudinal electric field starts up from the round-off errors. Since the wave generation mechanism is resonant, the wave grows secularly until non-linear effects cause plasma wave breaking and limit thus the plasma wave growth around $t = 90\omega_p^{-1}$. From Figs. 5–9 we can observe the distribution function (on the right) in the phase-space (x, p_x) and its relative adaptive phase-space grid (on the left). When the plasma wave rises, the formation of phase-space vortices is clear

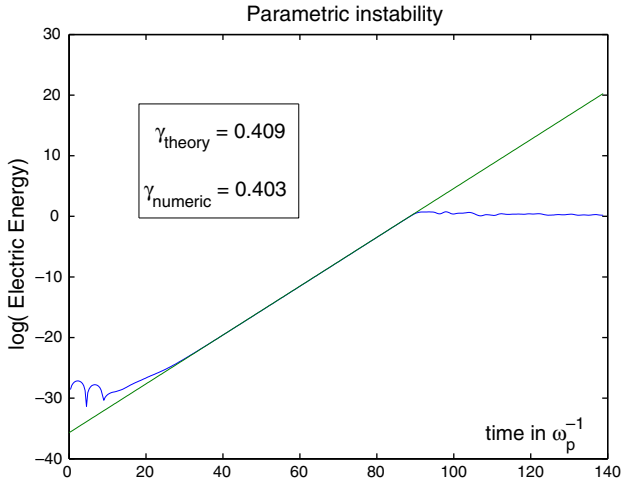

Fig. 4. Growth rate of the parametric instability.

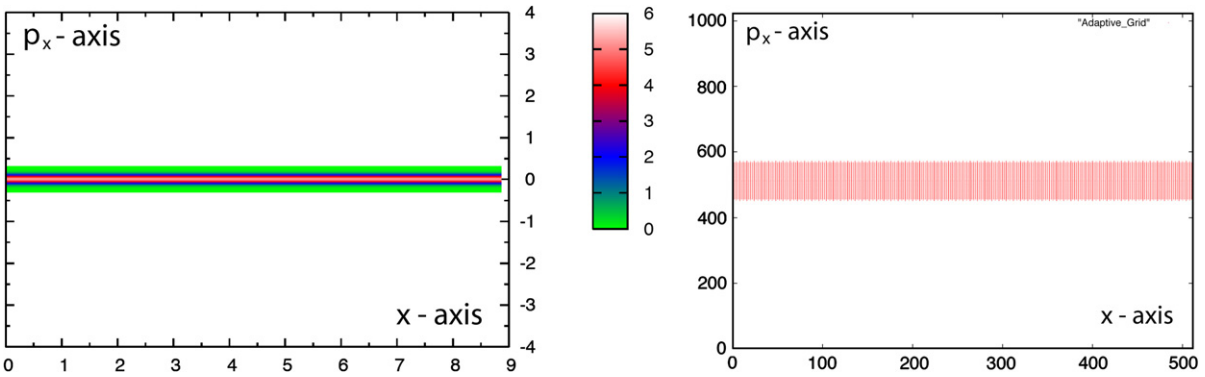

Fig. 5. Snapshots at $t = 0\omega_p^{-1}$ of the distribution function in phase-space (x, p_x) and the associated adaptive grid for the parametric instability.

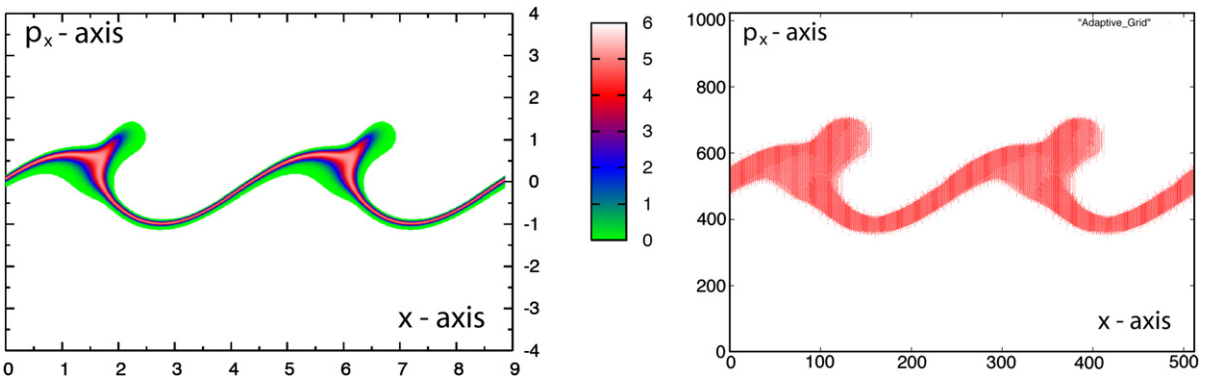

Fig. 6. Snapshots at $t = 90.24\omega_p^{-1}$ of the distribution function in phase-space (x, p_x) and the associated adaptive grid for the parametric instability.

in Fig. 5, and, when the plasma wave fields saturates, plasma wave breaking becomes evident at time $t = 93.71$, with occurring of a particle acceleration. In Figs. 5 (right) to 7 (right), we observe that the refined domain (in

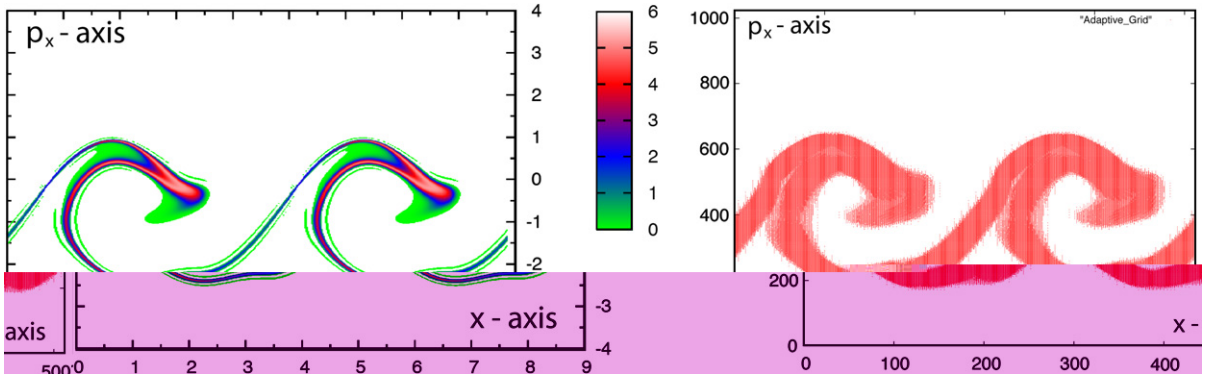

Fig. 7. Snapshots at $t = 93.71\omega_p^{-1}$ of the distribution function in phase-space (x, p_x) and the associated adaptive grid for the parametric instability.

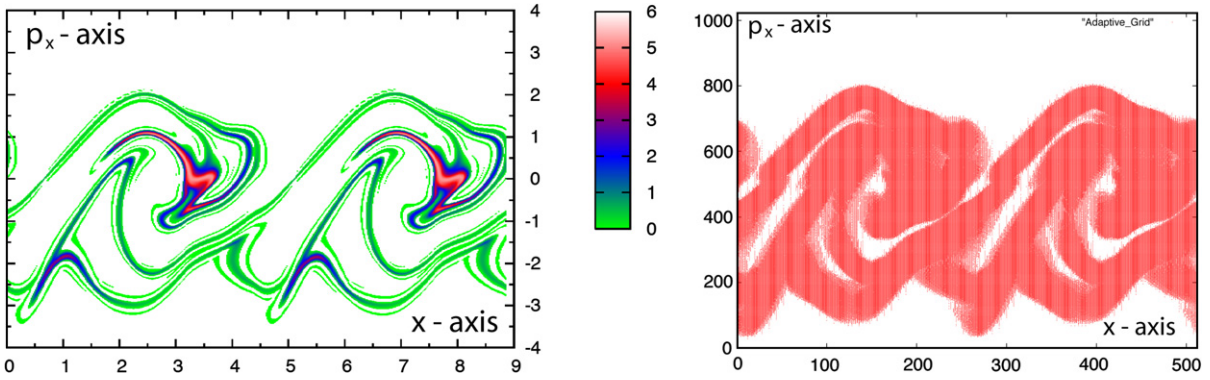

Fig. 8. Snapshots at $t = 100.65\omega_p^{-1}$ of the distribution function in phase-space (x, p_x) and the associated adaptive grid for the parametric instability.

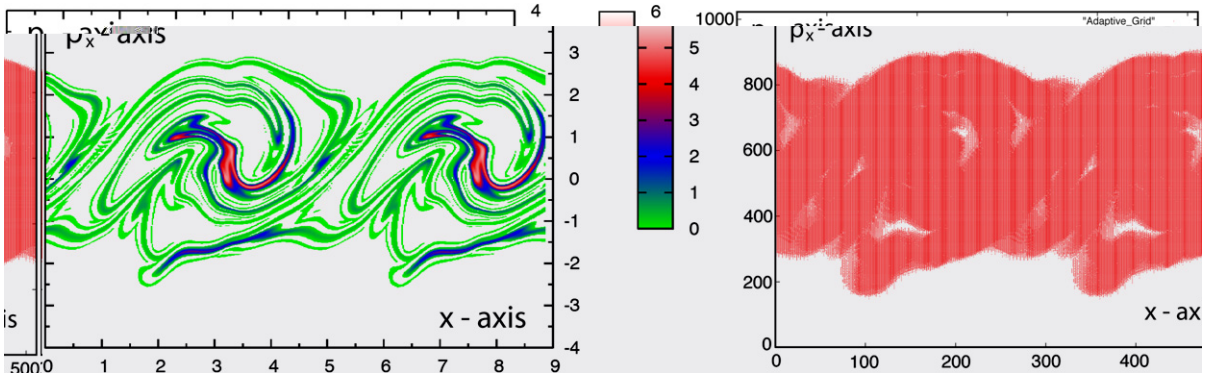

Fig. 9. Snapshots at $t = 104.13\omega_p^{-1}$ of the distribution function in phase-space (x, p_x) and the associated adaptive grid for the parametric instability.

red) is smaller than the unrefined domain (in white) which would have to be computed in the case of a non-adaptive numerical method. Here we see clearly the advantage of the adaptive scheme in term of memory space and CPU time saving. From Figs. 8 (right) to 9 (right) we see that the total domain of computation

starts to be filled by refinement points, thus the adaptive method is no more competitive compared to a numerical method where the phase-space is discretized with a fixed mesh.

6.2. Self-induced transparency and KEEN waves

In this test case we require a realistic bounded plasma layer (slab) with transparent walls. The electron distribution function is fixed at the boundaries by $f(t,x,p_x)=0$ for $x=0$ or $x=L$. The electromagnetic radiations are allowed to enter the system at the left boundary, when exiting at the other boundary, they do not return and are no longer considered. For right circularly polarized electromagnetic fields, we assume

$$E^+(t,x=0)=2E_0\mathrm{prof}(t)\cos(\omega_0 t),\qquad E^-(t,x=0)=0,$$
$$F^+(t,x=0)=0,\quad F^-(t,x=0)=-2vE_0\mathrm{prof}(t)\sin(\omega_0 t),$$

and for the potential vector

$$A_y(t,x=0)=-\frac{E_0}{\omega_0}\mathrm{prof}(t)\sin(\omega_0 t),\quad A_y(t,x=0)=-v\frac{E_0}{\omega_0}\mathrm{prof}(t)\cos(\omega_0 t),$$

in which the rise time profile prof is given by $\mathrm{prof}(t)=\sin^2(\pi t)/2\tau$ for $t\leqslant\tau$ and $\mathrm{prof}(t)=1$ for $t\geqslant\tau$ (and $\tau=50\omega_p^{-1}$). It is well-known that a high-frequency electromagnetic wave, with frequency less than the electron plasma wave ($\omega_0<\omega_p$) cannot propagate in a plasma. Nevertheless, if the intensity of the pump wave is sufficiently intense to make the electrons relativistic, the cutoff frequency decreases due to relativistic mass variation (increasing of the Lorentz factor). In the following, a laser pulse propagation in the x-direction is normally incident on an inhomogeneous density profile in the case of an overdense plasma. In the present simulations, the ions form an immobile background with steep gradient in density and the electron density is taken such that $n_0/n_c=1.20$. The normalized quiver momentum is $a_0=1.25$. The physical system consists of a plasma layer of uniform density of length $L_{\mathrm{plasma}}=60c/\omega_p$, surrounded by a vacuum region of length $L_{\mathrm{vacuum}}=60c/\omega_p$ on both sides. The total length of the system is then $L=L_{\mathrm{plasma}}+2L_{\mathrm{vacuum}}+2L_{\mathrm{jump}}=210c/\omega_p$ where $L_{\mathrm{jump}}=15c/\omega_p$ is a small region over which the density jumps from zero to n_0. The initial condition for electron distribution is a Maxwellian equilibrium with $T_{\parallel}=20$ keV. For the sampling of the phase-space we choose a coarse grid $N_xN_{p_x}=256\times 64$ with the possibility to refine the mesh adaptively on three more level in each direction. The threshold ϵ_0 is set to 10^{-8}. The time step is set to $\Delta t=0.1025$. In a first penetration phase of the laser pulse (on the time interval $[0,550\omega_p^{-1}]$), a relativistic Doppler shift takes place at the moving wave front (which acts as a moving mirror) and causes the beating on incoming pump wave with its reflected Doppler-shifted wave (from Figs. 10–12 (left)). The beating of this pump with its reflected wave from the front wave (area where there is a discontinuity of the plasma density) leads to the formation of vortices (~11 vortices). As a result a resonant three-wave parametric instability develops and gives rise to an electron acoustic-like(low-frequency) plasma wave which heats the plasma in a coherent way and generates the formation of trapping-like structures. This phenomenon is called self-induced transparency. Once the front wave (and the laser pulse) has crossed the plasma layer, the slab is under-

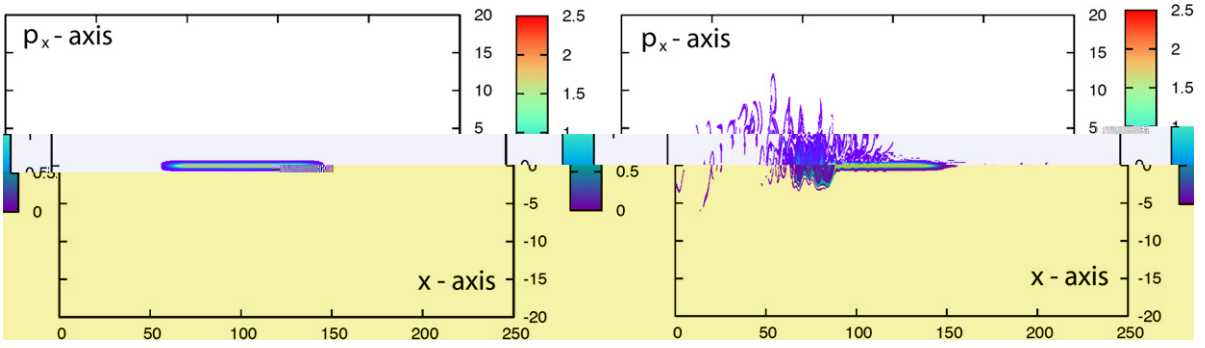

Fig. 10. Snapshots at $t=0\omega_p^{-1}$ (left) $t=205\omega_p^{-1}$ (right) of the distribution function in phase-space (x,p_x) for the self-induced transparency.

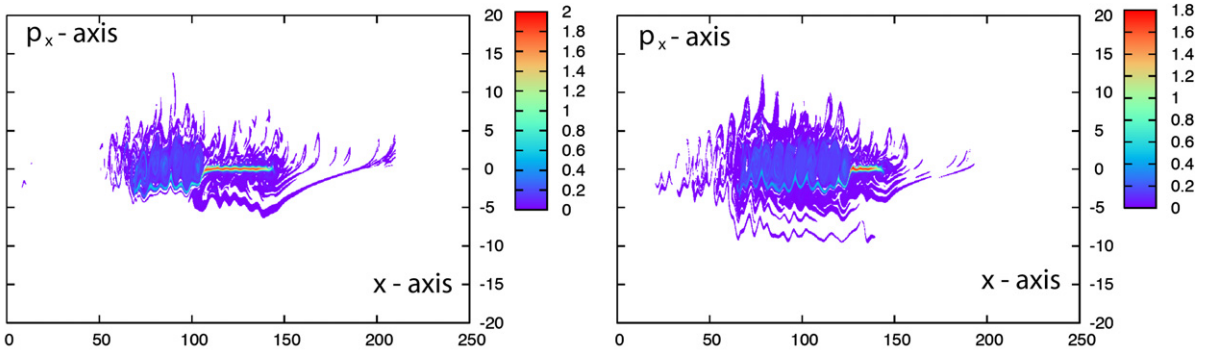

Fig. 11. Snapshots at $t = 307.6\omega_p^{-1}$ (left) $t = 414.1\omega_p^{-1}$ (right) of the distribution function in phase-space (x, p_x) for the self-induced transparency.

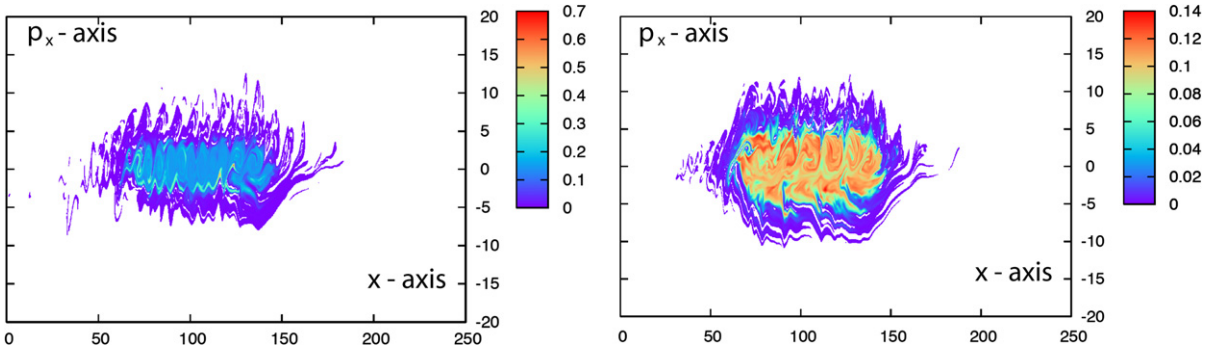

Fig. 12. Snapshots at $t = 512.6\omega_p^{-1}$ (left) $t = 922.8\omega_p^{-1}$ (right) of the distribution function in phase-space (x, p_x) for the self-induced transparency.

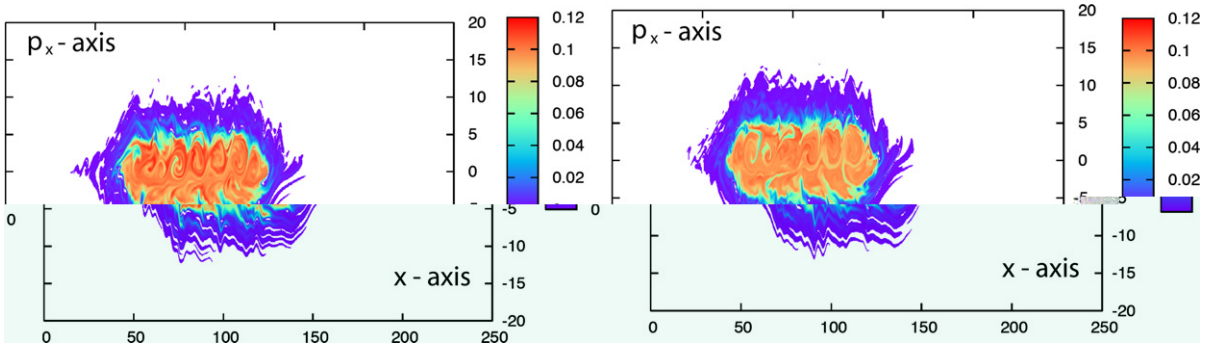

Fig. 13. Snapshots at $t = 1128\omega_p^{-1}$ (left) $t = 1333\omega_p^{-1}$ (right) of the distribution function in phase-space (x, p_x) for the self-induced transparency.

dense and transparent for light and thus another physical process takes place. When the relativistic Doppler shift ceases, a new three-wave parametric instability occurs involving the decay of the pump wave into a scattered radiating slab mode (called "weakly radiating pseudo-cavity electromagnetic mode"), close to plasma frequency, and a low-frequency plasma wave called KEEN wave (kinetic electron electrostatic non-linear waves) [1,26]. The trapping structures, seen in the phase-space (Figs. 12 (right) to 13), is associated to the exci-

tation of this kinetic self-sustained non-linear electron mode (KEEN wave). They represent a non-steady variant of the well-known Bernstein–Greene–Kruskal (BGK) modes [3] that describe invariant traveling electrostatic waves in plasmas. This KEEN mode can be excited in a sufficiently hot plasma and with sufficiently intense fields. Therefore we see the importance of preliminary beatwave mechanism, induced by Doppler shift, which has strongly heated the plasma during the self-induced transparency stage. In Fig. 13 we see the formation of a strong return current and the traveling of vortices which disappear in a return current when they reach the right side of the slab and which reappear from the return current on left side of the plasma slab ($\sim$7 vortices). The stimulated KEEN slab scattering (SKSS) process plays an important role in the mechanism of plasma heating to relativistic temperatures. This results are similar to those obtained in [25,26].

In Fig. 10, we observe that the region, where the plasma density is non-zero, is smaller than the whole domain of computation displayed in Figs. 10–14. We have to take a box with a great part of vacuum because the propagation of electromagnetic waves through the plasma leads to the formation of thin and localized filaments of accelerated particles (see Fig. 11) which can spread over all the box length. Therefore, we understand why in this typical situation an adaptive algorithm should be more interesting than a uniform one.

6.3. Laser wake-field

In this test case we are interested in the laser wake-field process, which seems to be a good way to accelerate particles to very relativistic velocities [23]. The laser pulse which has a Gaussian profile in time, is ultra-intense and has a ultra-short wave length. It enters at the left boundary of the simulation box, propagates first into

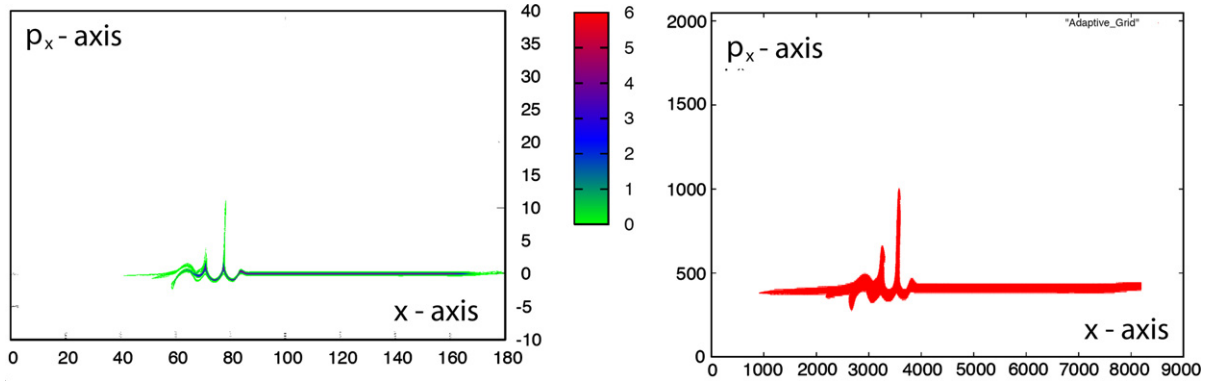

Fig. 14. Snapshots at $t = 88\omega_p^{-1}$ of the distribution function in phase-space (x, p_x) and the associated adaptive grid for the laser wake-field.

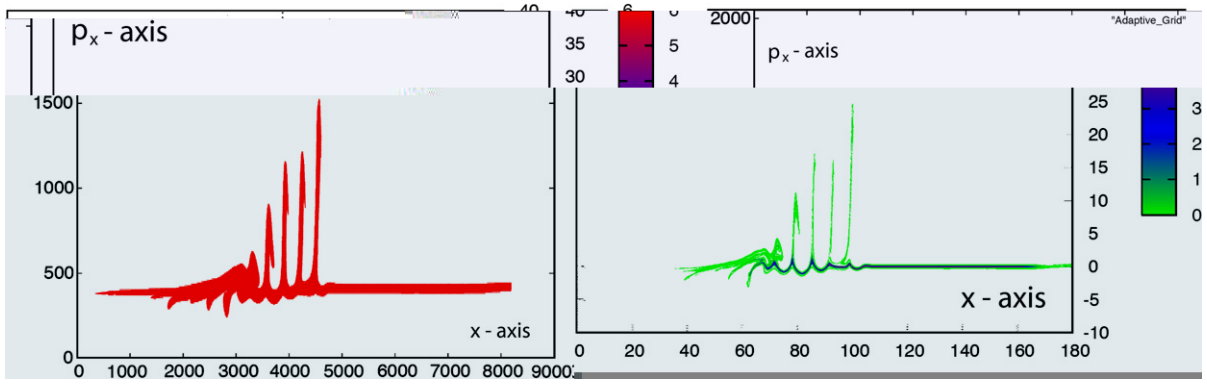

Fig. 15. Snapshots at $t = 110\omega_p^{-1}$ of the distribution function in phase-space (x, p_x) and the associated adaptive grid for the laser wake-field.

vacuum before penetrating an underdense plasma slab. The acceleration will be maximum if the ponderomotive force pushes the electron over a length equal to $\lambda_p/2$ (where λ_p is the plasma wave length) and if they are slowing down over the same length. Therefore we need a pulse of width $\tau = 2\pi/\omega_p$, and thus the electrons oscillate at the plasma frequency ω_p. Here we suppose that the ions form a fixed inhomogeneous neutralizing background. As in Section 6.2, the initial distribution of the electrons is a Maxwellian distribution in longitudinal momentum with a temperature of 3 keV, modulated in space by an inhomogeneous density. The initial condition for the electromagnetic fields $E^{\pm}$, $F^{\pm}$ and $\mathbf{A}_{\perp}$ are the same as in Section 6.2 except that now the profile prof is Gaussian, i.e. $\mathrm{prof}(t) = \exp(-\alpha(t-\tau/2)^2)$ for $t \leqslant \tau$ and $\mathrm{prof}(t) = 0$ for $t > \tau$. The bandwidth of this pulse is $\Delta = 2\sqrt{1/\alpha}$ where $\alpha = (2\omega/\pi)^2$. In this case the pulse is chosen such that $\exp(-\alpha(\tau/2)^2) \ll 1$, which is satisfied for $\tau = 2\Delta = 2\pi/\omega_p$. The total length of the system is then $L = L_{\mathrm{plasma}} + L_{\mathrm{vacuum,right}} + L_{\mathrm{vacuum,left}} + 2L_{\mathrm{jump}} = 180c/\omega_p$ with $= L_{\mathrm{plasma}} = 90$, $L_{\mathrm{vacuum,right}} = 10$, $L_{\mathrm{vacuum,left}} = 60$ and $2L_{\mathrm{jump}} = 20$. In the simulation the circularly polarized laser pulse has a quiver momentum $a_0 = \sqrt{3/2}$ and the density of the plasma is such that $n_0/n_c = 0.1$. The phase-space is sampled with a coarse grid $N_x N_{p_x} = 1024 \times 256$ and with the possibility to refine the mesh adaptively on three more levels in each direction. The threshold ϵ_0 is set to 10^{-8}.

The ponderomotive force associated to the laser pulse pushes the electrons forward and the response of the plasma is the generation of a longitudinal electric field which tends to cancel this movement. During its propagation into the plasma, the laser pulse will leave in its wake a longitudinal electric wave of phase velocity $v_\varphi \approx c$ and wave length λ_p. From Figs. 14–18, we can observe the modulation of the distribution function in the phase-space (x, p_x) at different times. In Fig. 14 the peak of the distribution function is typically asso-

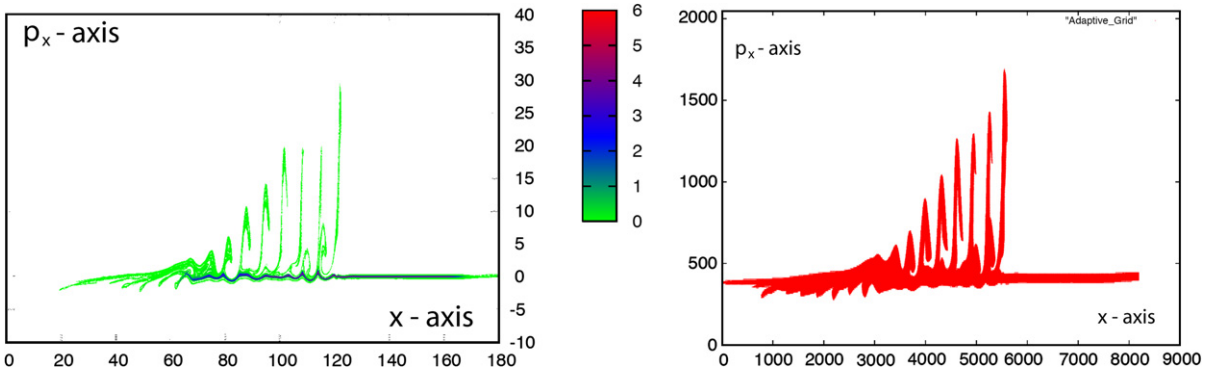

Fig. 16. Snapshots at $t = 132\omega_p^{-1}$ of the distribution function in phase-space (x, p_x) and the associated adaptive grid for the laser wakefield.

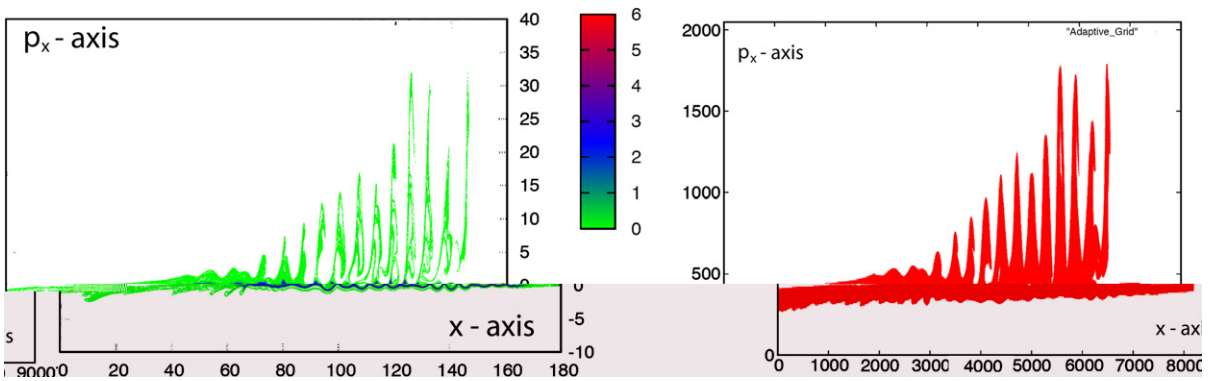

Fig. 17. Snapshots at $t = 176\omega_p^{-1}$ of the distribution function in phase-space (x, p_x) and the associated adaptive grid for the laser wakefield.

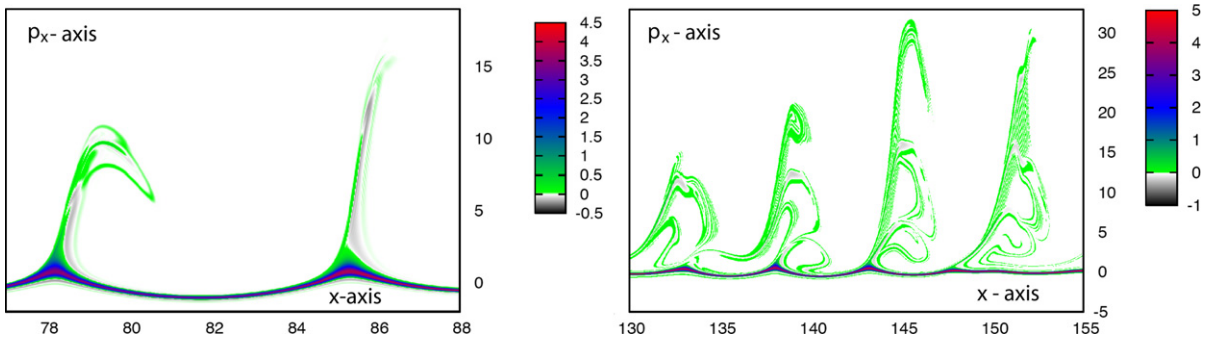

Fig. 18. Zoom of Figs. 15 and 16.

ciated to the wavebreaking process, which is followed by the acceleration of the electrons. In Figs. 15–17, we see clearly a strong acceleration of the plasma electrons in the laser pulse wake-field, up to moment value $p_x/mc = 30$. In Fig. 17 and 18 (right) we observe particle trapping processes which occur from position $x\omega_p/c = 110$ to position $x\omega_p/c = 160$ at the time $t = 176\omega_p^{-1}$. In Fig. 18 (left) we see that the electrons are well accelerated along a straight line as can be also reproduced by a PIC code [39,42]. Therefore our adaptive scheme can depict the same thin filaments as PIC codes do, whereas it could be almost impossible with a fixed mesh of phase-space because of the huge needs of CPU time and memory capacity. Then the advantage of the adaptivity compared to classical Eulerian numerical method constructed on a fixed mesh is that you can observe and follow in time the fine structures like these narrow localized filaments of accelerated particles with a reduced computation cost and with weak memory storage. Let us note that in Figs. 14 (right) to 17 (right) the whole region (white and red areas) corresponds to the finest grid we would have to compute with a non-adaptive Eulerian numerical method.

6.4. Performance analysis

The performance analysis presented in this section has been carried out on the zahir machine (IBM eServer p690, p690+, & p655) at IDRIS (Institut du Développement et des Ressources en Informatique Scientifique, CNRS, France). The zahir computer is a scalable distributed and shared memory multi-processor system of 1024 processors Power4 and Power4+. With a frequency equal to 1.3 GHz, the theoretical peak performance is 5.2 Gflop/s per processor. The level 1 instruction have a size of 64 KB and data cache have a size of 32 KB, whereas the secondary unified instruction/data cache size is 1.5 MB. Even if our adaptive semi-Lagrangian scheme is implemented in a parallel version, all runs have been performed with one processor, in order to measure the efficiency of each numerical algorithm itself and not the parallelization method. For a representative test case, we present computation time in seconds at one particular time step within a simulation of 1600 time steps. We compare the computation time given by two numerical schemes. The first one, named adaptive-S.-L., is the adaptive semi-Lagrangian scheme depicted in this paper and the second one, called uniform-S.-L., is the semi-Lagrangian scheme described in Reference [38]. In the article [38], a semi-Lagrangian scheme is developed on a uniform grid of phase-space while the interpolation at the origin of the characteristics – computed as the solution of a fixed-point problem solved by a Newton algorithm – is performed with cubic splines inter-

Table 4
Computation time in seconds for the adaptive-S.-L. scheme and the uniform-S.-L. scheme for the three test cases ILPP%RPI, ILPO%SIT and ILPO%LWF, after 1600 time steps

Test case	Scheme	
	Adaptive-S.-L.	Uniform-S.-L.
ILPP%RPI	3000s (50m)	5280s (1h28m)
ILPO%SIT	6060s (1h41m)	8220s (2h17m)
ILPO%LWF	23760s (6h36m)	32992s (9h10m)

polation. The labels ILPP%RPI, ILPO%SIT and ILPO%LWF refer respectively to the test case 6.1, 6.2 and 6.3. For the test case ILPP%RPI, the adaptive algorithm starts with a distribution function of $2^6 \times 2^{10}$ points at level $\mathring{j}_x = 6, \mathring{j}_{p_x} = 10$, with three levels of refinement and a threshold $\epsilon_0 = 10^{-6}$. We denote this adaptive grid as $2^{6+3} \times 2^{10+3}$. In the test case ILPO%SIT we take the adaptive grid $2^{8+3} \times 2^{8+3}$ and a threshold ϵ_0 set to 10^{-8}. Let us note that the corresponding grid size for the uniform-S.-L. scheme is of $2^{11} \times 2^{11}$ points. For the last test case ILPO%LWF the threshold ϵ_0 is set to 10^{-8} and the adaptive grid is $2^{10+3} \times 2^{8+3}$. The computation times are summarized in Table 4.

7. Conclusion and discussion

To conclude several remarks must be pointed out:

As a matter of fact the purely collective approach – as the Vlasov model – is an approximation of the N body problem: a plasma of length L allows $(L/\lambda_D)^3$ collective modes while the importance of the individual effects is given by the parameter $n_0\lambda_D^3$ (n_0 being the density of particles). In fusion and space plasma $n_0\lambda_D^3$ is of order of $10^6 - 10^9$ while $L/\lambda_D = 10^3 - 10^4$. Obviously we cannot treat 10^{18} particles (since $N = n_0\lambda_D^3(L/\lambda_D)^3$ this number corresponds to $L/\lambda_D = 10^3$ and $n_0\lambda_D^3 = 10^9$). Indeed the Vlasov approach (corresponding to $n_0\lambda_D^3 \to +\infty$) if it deals with the correct treatment of the purely collective plasma does it by introducing a phase-space, i.e. a product of the configuration space by the velocity space. This guarantees the noiseless character of the model.

The next important aspect is then the loss of efficiency of the Vlasov model when filamentation in velocity space arises. The first different attempts on the numerical solution of the Vlasov equation (especially with spectral methods like Fourier–Hermite see [28]) were not able to solve the problem of filamentation unless using a huge number of Hermite polynomials. For some problems encountered in high intensity laser–plasma interaction such as the laser wake-field accelerator or the parametric instabilities in the relativistic regime, we have to simulate large beams located in very thin regions of the phase-space while large regions are empty of particles. Very fine grids are then needed. For such problems, the use of an adaptive mesh method (with a natural criterion to perform local grid refinements) allows to compensate the efficiency lost by the filamentation process. It should also be noted that in first non-adaptive 2D causal Vlasov simulations [27] the case of laser–plasma interaction have shown that the particle acceleration arises in the longitudinal direction (which corresponds to the direction of laser propagation, say $x - p_x$) while only modulation of f is just observed in the transverse $y - p_y$ phase-space plane. A very fine resolution of the plane $x - p_x$ is then required to obtain a good description of the accelerated particle dynamics. The adaptive mesh scheme used here allows such a description.

Another important aspect was the number of dimensions which can be handled. The border between both methods (PIC and Vlasov) consequently is given by the phase-space dimension and more precisely the velocity space dimension.

Indeed in PIC modes, particles are considered as volume elements of the phase-space gathered at the same point $(\mathbf{r}_i, \mathbf{p}_i)$. In that respect an individuality parameter will show up. An efficient smoothing is then introduced either by considering overlapping particles which are extended in space, or by filtering the short wavelengths of the fields or by redistributing the charge of a superparticle among the neighboring points of the configuration mesh. Although these treatments decrease efficiently the unwanted – because exaggerated – individual effects, they do not change the scaling of these effects and dividing these effects by two still imposes a doubling of the number of particles. The reason is that, to kill these effects we must smooth the fields not only on the inter particle distance but also on the Debye length, but then we begin to modify the possible collective behavior: finally $n_0\lambda_D^d$ of order 10^3or even 10^4 must be used, which correspond to small values of the graininess parameter. Actually Vlasov codes can be preferred for $2d + 1v$ (2D in configuration space plus one-dimension in velocity or 3D phase-space) or $3d + 1v$, or even $2d + 2v$ (4D phase-space) problems. It is the velocity space sampling which plays here the major role since usually the resolution of the Maxwell's equations requires the same sampling in the configuration space in both Lagrangian and Eulerian Vlasov models. An adaptive mesh method in the semi-Lagrangian approach allows to take into account two-dimensions in velocity since the computational effort is put only on these non-zero regions of the velocity space. PIC codes are however very efficient in particle acceleration provided that the (physical) graininess parameter is not too small, since

particles were found – during their evolution – located exactly along the fine filaments which characterize the physical particle acceleration process. However the bad sampling of the velocity is worst in the region of low density and high velocity where there are very few particles which play an important role in the evolution of the plasma (stopping of the Landau damping by non-linear effects, heating process, ...). The adaptive mesh methods may in these cases considerably increase the efficiency of the Vlasov model without modifying its advantages (noiseless character and good resolution in phase-space as observed in the numerical tests).

An interesting point is the existence of dynamical invariants as shown in Section 3. If we take these invariants as new independent variables, then we can discretize them coarsely, since there is no exchange of particles between the different populations (they simply interact through the electromagnetic fields). Providing a special choice of initial conditions, they remain exact for all time t and space x. From both an analytical and numerical point of view the use of exact invariants allows obviously a reduction of the complexity of dealing with a full Vlasov equation with a 3D velocity space. This makes the use of an adaptive mesh scheme a very powerful method when it is coupled with such invariants (transverse canonical invariants met in laser–plasma interaction or adiabatic invariants in gyrokinetic models). The performance and accuracy obtained in the examples presented here are very satisfying and these examples show that our adaptive Vlasov scheme is able to describe accurately non-linear effects such as the filamentation process – which is a very difficult problem to solve from the numerical point of view – or the saturation mechanism of the parametric instabilities in the relativistic regime.

Even though the use of an adaptive mesh in a semi-Lagrangian Vlasov solver will eventually be of benefit as well in terms of memory as in computational cost for many problems in plasma physics and in beam physics, the development and implementation of an efficient adaptive solver is a complex problem that will still need much collaborative effort between physicists, applied mathematicians and computer scientists. Indeed, in the problems that were addressed in this paper, as in many other problems involving the Vlasov equation, the number of grid points that remain with our wavelet adaption technique after some time becomes too high for the method to be competitive with a uniform mesh solver due to the important overhead associated to the wavelet method which gives us the adaptive grid. This difficulty becomes even more important for a parallel version of the code. There are now efficient uniform grid Vlasov solvers that scale very well on thousands of processors whereas the efficient parallelization of adaptive mesh solvers is a real challenge.

Here the Vlasov simulations are performed in a two-dimensional phase-space where the development of thin filaments, strongly amplified by relativistic effects, is the signature of strong particle acceleration in laser–plasma interaction. The phase-space filamentation requires an important increase of the total number of points of the phase-space grid as the filaments get finer as time goes on. The structure of these filaments is essentially one-dimensional even in higher dimensions. Therefore, the adaptive method could be more useful and efficient in cases where these thin filaments that need to be resolved are a very small fraction of the hypervolume, which arises in higher dimensions because of the surface-to-volume scaling and the essentially one-dimensional structure of the filaments.

The main drawback of our scheme is the poor local character – in phase-space – of the semi-Lagrangian method and the wavelet multiscale reconstruction that we have used. Indeed the lack of space locality of the semi-Lagrangian method comes from the characteristic curves tracking which prevents us to know a priori the size of the dependance domain of each mesh point and thus the number of cells that the characteristics will cross. The poor locality of interpolets comes from the size of its support. This poor locality of the scheme has two negative consequences on the efficiency of the adaptive method. The first one is that the scheme involves more points than it is needed. The second one is that it is difficult to construct an efficient parallel algorithm such as domain decomposition algorithm. Therefore, the main way to improve the efficiency of the adaptive method is to increase the local character in phase-space of the numerical scheme, by considering multiscale reconstruction with more compact support and by replacing the semi-Lagrangian method with more local – in space – numerical schemes as compact finite difference schemes, discontinuous-Galerkin method or finite element residual schemes which are well suited for parallel domain decomposition techniques.

References

[1] B.B. Afeyan, K. Won, V. Savchenko, T.W. Johnston, A. Ghizzo, P. Bertrand, Kinetic electrostatic electron nonlinear waves and their interactions driven by the ponderomotive force of crossing laser beams, in: B. Hammel, D. Meyer-Hofer, L. Meyer-ter-Vehn, H. Azechi (Eds.), Proceeding of the Third International Conference on Inertial Fusion Sciences and Applications MO34, Monterey, California, 2003, American Nuclear Society, LaGrange Park, IL, 2004, p. 213.

[2] A.I. Akhiezer, R.V. Polovin, Theory of wave motion of an electron plasma, Sov. Phys. JETP 3 (1956) 696–705.

[3] I.B. Bernstein, J.M. Greene, M.D. Kruskal, Exact non linear plasma oscillations, Phys. Rev. 108 (1957) 546–550.

[4] M.L. Bégué, A. Ghizzo, P. Bertrand, E. Sonnendrücker, O. Coulaud, Two-dimensional semi-Lagrangian Vlasov simulations of laser–plasma interaction in the relativistic regime, J. Plasma Phys. 62 (1999) 367–388.

[5] S. Bertoluzza, An adaptive collocation method based on interpolating wavelets, Multiscale Wavelet Methods for Partial Differential Equations, Wavelet Anal. Appl., vol. 6, Academic Press, San Diego, CA, 1997, pp. 109–135.

[6] N. Besse, F. Filbet, M. Gutnic, I. Paun, E. Sonnendrücker, An adaptive numerical method for the Vlasov equation based on a multiresolution analysis, in: F. Brezzi, A. Buffa, S. Escorsaro, A. Murli (Eds.), Numerical Mathematics and Advanced Applications, Springer, 2003, pp. 437–446, ENUMATH 2001.

[7] N. Besse, Etude mathématique et numérique de l'équation de Vlasov non linéaire sur des maillages non structurés de l'espace des phases, Ph.D. Thesis, Publication de l'Institut de Recherche Mathématique Avancée, Université Louis Pasteur, Strasbourg, 2003.

[8] N. Besse, E. Sonnendrücker, Semi-Lagrangian schemes for the Vlasov equation on an unstructured mesh of phase space, J. Comput. Phys. (2003) 341–376.

[9] N. Besse, J. Segré, E. Sonnendrücker, Semi-Lagrangian schemes for the two-dimensional Vlasov–Poisson system on unstructured meshes, Transport Theor., Statist. Phys. 34 (2005) 311–322.

[10] C.K. Birdsall, A.B. Langdon, Plasmas Physics via Computer Simulation, McGraw-Hill, 1985.

[11] C.Z. Cheng, G. Knorr, The integration of the Vlasov equation in configuration space, J. Comput. Phys. 22 (1976) 330–351.

[12] A. Cohen, Numerical Analysis of Wavelets Methods, Studies in Mathematics and its Applications, vol. 32, North-Holland, 2003.

[13] A. Cohen, S.M. Kaber, S. Mueller, M. Postel, Fully adaptive multiresolution finite volume schemes for conservation laws, Math. Comput. 72 (2003) 183–225.

[14] A. Cohen, I. Daubechies, J.C. Feauveau, Biorthogonal bases of compactly supported wavelets, Commun. Pure Appl. Math. 45 (1992) 485–560.

[15] I. Daubechies, Ten lectures on wavelets, Series in Appl. Math., vol. 61, Society for Industrial and Applied Mathematics, Philadelphia, 1992.

[16] R. Devore, B. Lucier, High order regularity for conservation laws, Indiana Math. J. 39 (1990) 413–430.

[17] R.C. Davidson, N.A. Krall, Vlasov description of an electron gas in a magnetic field, Phys. Rev. Lett. 22 (1969) 833–837.

[18] R.C. Davidson, N.A. Krall, Vlasov equilibria and stability of an electron gas, Phys. Fluids 13 (1970) 1543–1555.

[19] R.C. Davidson, Electrostatic shielding of a test charge in a non-neutral plasma, J. Plasma Phys. 6 (1971) 229–235.

[20] D. Deslauriers, D. Dubuc, Dyadic interpolation, in: Fractals, dimensions non entières et applications, Masson, Paris, 1987, pp. 44–55.

[21] D. Deslauriers, D. Dubuc, Symmetric iterative interpolation processes, Constr. Approx. 5 (1989) 49–68.

[22] N. Dyn, J.A. Gregory, D. Levin, A four point interpolatory subdivision scheme for curves design, Comput. Aided Geom. Des. 4 (1987) 257–268.

[23] E. Esarey, P. Sprangle, J. Krall, A. Ting, Overview of plasma-based accelerator concepts, IEEE Trans. Plasma Sci. 24 (1996) 252–288.

[24] D.W. Forslund, J.M. Kindel, E.L. Lindman, Plasma simulation studies of stimulated scattering processes in laser-irradiated plasmas, Phys. Fluids 18 (1975) 1017–1030.

[25] A. Ghizzo, D. Del Sarto, T. Réveillé, N. Besse, R. Klein, Self-induced transparency scenario revisted via beating-wave heating induced by Doppler shift in overdense plasma layer, Phys. Plasmas 14 (2007) 062702.

[26] A. Ghizzo, T.W. Johnston, T. Réveillé, P. Bertrand, M. Albrecht-Marc, Stimulated-Raman-scatter behaviour in a relativistically hot plasma slab and an electromagnetic low-order pseudocavity, Phys. Rev. E 74 (2006) 046407.

[27] A. Ghizzo, F. Huot, P. Bertrand, A non periodic 2D semi-Lagrangian Vlasov code for laser–plasma interaction on parallel computer, J. Comput. Phys. 186 (2003) 47.

[28] F.C. Grant, M.R. Feix, Fourier–Hermite solutions of the Vlasov equations in the linearized limit, Phys. Fluids 10 (1967) 696–702.

[29] S. Guérin, G. Laval, P. Mora, J.C. Adam, A. Héron, A. Bendid, Modulational and Raman instabilities in the relativistic regime, Phys. Plasmas 2 (1995) 2807–2814.

[30] S. Guérin, P. Mora, J.C. Adam, A. Héron, G. Laval, Propagation of ultra-intense laser pulses through overdense plasma layers, Phys. Plasmas 3 (1996) 2693–2701.

[31] M. Gutnic, M. Haefele, I. Paun, E. Sonnendrücker, Vlasov simulations on an adaptive phase-space grid, Comput. Phys. Commun. 164 (2004) 214–219, ICNSP 2003.

[32] M. Gutnic, M. Haefele, E. Sonnendrücker, Moments conservation in adaptive Vlasov solver, Nucl. Instrum. Methods Phys. Res., Sect. A 558 (2006) 159–162, ICAP 2004.

[33] V. Grandgirard, M. Brunetti, P. Bertrand, N. Besse, X. Garbet, P. Ghendrih, G. Manfredi, Y. Sarazin, O. Sauter, E. Sonnendrücker, J. Vaclavik, L. Villard, A drift-kinetic semi-Lagrangian 4D code for ion turbuence simulation, J. Comput. Phys. 217 (2006) 395–423.

[34] M. Griebel, F. Koster, Adaptive wavelet solver for the unsteady incompressible Navier–Stokes equations, in: J. Maleck, J. Necas, M. Rokyta (Eds.), Advances in Mathematical Fluid Mechanics, Springer Verlag, 2000.

[35] M. Haefele, G. Latu, M. Gutnic, A parallel Vlasov solver using a wavelet based adaptive mesh refinement, Parallel Processing, 2005, ICPP 2005 Workshop, International Conference Workshop on, IEEE Conferences Proceedings.

[36] A. Harten, Multiresolution algorithms for the numerical solution of hyperbolic conservation laws, Commun. Pure Appl. Math. 48 (1995) 1305–1342.
[37] F. Huot, A. Ghizzo, P. Bertrand, E. Sonnendrücker, O. Coulaud, Study of propagation of ultraintense electromagnetic wave through plasma using semi-Lagrangian Vlasov codes, IEEE Trans. Plasma Sci. 28 (2000) 1209–1223.
[38] F. Huot, A. Ghizzo, P. Bertrand, E. Sonnendrücker, O. Coulaud, Instability of the time splitting scheme for the one-dimensional and relativistic Vlasov–Maxwell system, J. Comput. Phys. 185 (2003) 512–531.
[39] C. Josh, C.E. Clayton, W.B. Mori, J.M. Dawson, T. Katsouleas, The prospects for a GeV plasma beat wave accelerator, Plasma Phys. Contr. Fus. 16 (1994) 65–77.
[40] G. Manfredi, M. Shoucri, M. Feix, P. Bertrand, E. Fijalkow, A. Ghizzo, The numerical integration of the Vlasov equation possessing an invariant, J. Comput. Phys. 121 (1995) 298–313.
[41] T. Nakamura, T. Yabe, Cubic interpolated propagation scheme for solving the hyper-dimensional Vlasov–Poisson equation in phase space, Comput. Phys. Commun. 120 (1999) 122–154.
[42] L.O. Silva, M. Marti, J.R. Davies, R.A. Fonseca, C. Ren, F.S. Tsung, W.B. Mori, Proton shock acceleration in laser–plasma interactions, Phys. Rev. Lett. 92 (2004) 015002.
[43] E. Sonnendrücker, J. Roche, P. Bertrand, A. Ghizzo, The semi-Lagrangian method for the numerical resolution of Vlasov equation, J. Comput. Phys. 149 (1996) 841–872.
[44] W. Sweldens, The lifting scheme: a construction of second generation wavelets, SIAM J. Math. Anal. 29 (2) (1998) 511–546.
[45] T. Tajima, J.M. Dawson, Laser electron accelerator, Phys. Rev. Lett. 43 (1979) 267–270.
[46] S. Weber, C. Riconda, V.T. Tikhonchuck, Strong kinetic effects in cavity-induced low-level saturation of stimulated Brillouin backscattering for high-intensity laser–plasma interaction, Phys. Plasmas 12 (2005) 43101.